



Incorporation mechanisms and infrared absorption coefficients of water in MgSiO₃ orthoenstatite clarified via comprehensive NMR and vibrational spectroscopic measurements, and first-principles calculations

Xianyu Xue¹ · Masami Kanzaki¹ · Abd-Erraouf Djirar² · Chris Gregson^{3,4}

Received: 13 November 2023 / Accepted: 27 February 2024 / Published online: 25 March 2024
© The Author(s) 2024

Abstract

We performed ¹H and ²⁹Si NMR and infrared measurements, and first-principles calculations to clarify the nature of OH defects in MgSiO₃ orthoenstatite. An orthoenstatite sample synthesized at 7 GPa and 1200 °C from a composition of MgSiO₃ + 0.1 wt% H₂O yielded two ¹H MAS NMR peaks near 5.9 and 7.6 ppm that are correlated in 2D NMR spectra, and two infrared bands near 3361 and 3066 cm⁻¹ that correspond to the previously reported A3 and A4 bands. The first-principles calculations confirmed that they are due to a pair of protons in a Mg (M2) vacancy. The previously reported A1 and A2 infrared bands near 3687 and 3592 cm⁻¹ for orthoenstatite synthesized at low silica activities were confirmed to arise from four protons in a SiB vacancy. The latter is predicted to give two additional OH stretching bands associated with two strongly hydrogen-bonded O3b-H bonds with frequencies below the spectral range reported thus far. The previously reported infrared absorption coefficients were thus revised to account for the undetected bands. ¹H NMR may be used to quantitatively detect all four protons (expected at 1–12 ppm). Other mantle minerals should also be examined for potentially overlooked OH defects with strong hydrogen bonding.

Keywords Water · Orthopyroxene · Hydrogen bonding · NMR · Vibrational spectroscopy · First-principles calculation

Introduction

Most of the Earth's water (up to several times or more of the present mass of the oceans) is believed to be stored in the deep mantle, possibly in the form of hydroxyl (OH) defects in nominally anhydrous major mantle minerals, such as

olivine, pyroxene and higher-pressure phases in the bulk mantle. Water is also transported into the deep mantle in the form of hydrous and nominally anhydrous minerals in subducting slabs, contributing to the dynamics of the Earth and the global water cycle that underpins Earth's habitability (cf., Keppler and Smyth 2006; Ohtani 2021; Peslier et al. 2017). Water as OH defects in nominally anhydrous minerals, even when present in trace amounts, can significantly change their melting temperature and various physical properties (e.g., electrical conductivity, diffusivity, elastic properties, sound velocity)(cf., Ingrin and Blanchard 2006; Jacobsen 2006; Karato 2006; Ohtani 2021; Yoshino and Katsura 2013). The effects of water on mineral properties strongly depend on how it is incorporated in the crystal structure (e.g., Keppler and Smyth 2006), and thus it is indispensable to understand the water incorporation mechanisms and solubility.

MgSiO₃ orthoenstatite is the Mg endmember of low-Ca orthopyroxene, the second most abundant mineral in the upper mantle. The crystal structure of MgSiO₃ orthoenstatite

Communicated by Dante Canil.

✉ Xianyu Xue
xianyu@misasa.okayama-u.ac.jp

¹ Institute for Planetary Materials, Okayama University, Yamada 827, Misasa, Tottori, Japan

² Department of Earth Sciences, Western University, London, ON, Canada

³ Department of Earth, Ocean and Ecological Sciences, University of Liverpool, Liverpool L69 3GP, UK

⁴ National Nuclear Laboratory, Central Laboratory, Sellafield, Seascale CA20 1PG, UK

(space group *Pbca*) consists of chains of SiO_4 tetrahedra running along the *c* direction, which are stacked back-to-back forming layers parallel to the (100) plane. There are two types of chains of SiO_4 tetrahedra (SiA and SiB) that are located in alternating silicate layers. Mg enters octahedral M sites forming edge-sharing chains that are parallel to the silicate chains. There are two types of M sites, the smaller M1 sites between apices of opposing silicate tetrahedra, and the larger M2 sites between bases of the silicate tetrahedra. At pressures above about 8 GPa at 1000 °C, orthoenstatite transforms to high-pressure clinoenstatite (space group *C2/c*), which is unquenchable and changes to low-pressure clinoenstatite (space group *P2₁/c*) upon decompression to ambient conditions (Pacalo and Gasparik 1990).

The solubility and incorporation mechanisms of water in MgSiO_3 orthoenstatite have been mostly studied by infrared (IR) spectroscopy so far (e.g., Grant et al. 2006; Prechtel and Stalder 2010; Rauch and Keppler 2002; Stalder et al. 2012). Rauch and Keppler (2002) determined the solubility of water in MgSiO_3 orthoenstatite at 0.2–7.5 GPa and 1100 °C using a starting material of nearly stoichiometric Mg/Si ratio with slight excess silica. The solubility was found to increase with pressure reaching 0.087(4) wt% H_2O (as determined by IR using the calibration of Bell et al. (1995) at 7.5 GPa and 1100 °C. Their reported IR absorption spectra contain two bands near 3363 and 3064 cm^{-1} , both strongly polarized parallel to the *c* axis, which were suggested to be likely due to a pair of protons associated with Mg vacancies. Stalder and coauthors reported IR absorption spectra on orthoenstatite synthesized at different pressures (4 to 8 GPa) and silica activities (Prechtel and Stalder 2010, 2011; Stalder et al. 2012). Two groups of bands were identified: two bands near 3687 and 3592 cm^{-1} (denoted as A1 and A2 band) show the strongest absorption for the polarization along the *a* axis, and two bands near 3362 and 3067 cm^{-1} (denoted as A3 and A4 band) show the strongest absorption for the polarization along the *c* axis, resembling those reported by Rauch and Keppler (2002). The relative integrated absorbance of the latter was found to increase with silica activity, and thus consistent with protons associated with Mg vacancies, and the former with those associated with Si vacancies.

However, the nature of such OH defects, especially those associated with Si vacancies, is not well understood. Balan et al. (2013) reported first-principles (FP) calculation results for OH defects associated with Mg and Si vacancies. They found that for two H atoms in a Mg vacancy (denoted $(2\text{H})_{\text{Mg}}$ hereafter), it is energetically more favorable for the 2H to reside in an M2 vacancy (denoted $(2\text{H})_{\text{M2}}$ hereafter) than in an M1 vacancy (denoted $(2\text{H})_{\text{M1}}$ hereafter). Their computed IR spectra for the $(2\text{H})_{\text{M2}}$ model match reasonably well in frequency and pleochroism with those of the observed A3

and A4 bands. For four H atoms in a Si vacancy (denoted $(4\text{H})_{\text{Si}}$ hereafter), they found that the substitution of the SiB site (denoted $(4\text{H})_{\text{SiB}}$ hereafter) is energetically more favorable than that of the SiA site (denoted $(4\text{H})_{\text{SiA}}$ hereafter). Their calculated IR spectra, however, do not agree with the experimentally observed ones. Sakurai et al. (2014) reported two configurations for the $(4\text{H})_{\text{SiB}}$ defects, but the relative stabilities were not given, and only part of the expected OH stretching bands were reported. Thus, the interpretation of the observed A1 and A2 bands for orthoenstatite remains an open question.

A reliable quantitative estimation of the water content by IR spectroscopy also requires a proper understanding of the band assignment, because the absorption coefficient often varies depending on the nature of the vibrating species (e.g., Bell et al. 1995; Libowitzky and Rossman 1997; Paterson 1982; Stalder et al. 2012), and OH stretching bands associated with strong hydrogen bonding may be too broad to detect at low concentrations (cf., Novak 1974; Xue et al. 2008).

Our previous study on Mg_2SiO_4 forsterite has shown that a combined approach of multi-nuclear (^1H , ^{29}Si) nuclear magnetic resonance (NMR) spectroscopic measurements and FP calculation is effective in unambiguously unraveling the incorporation mechanisms of water in a nominally anhydrous mineral (Xue et al. 2017b). ^1H magic angle spinning (MAS) NMR is intrinsically quantitative, and can be used to estimate the water content, regardless of the incorporation mechanism. The ^1H chemical shift is sensitive to the local environments, in particular, the hydrogen-bonding distance (cf., Xue and Kanzaki 2009). The peak shapes of ^1H static and MAS NMR spectra for clustered protons are sensitive to the ^1H - ^1H dipolar interactions, and thus can provide constraints on the number of protons and their configurations in the proton clusters. Furthermore, two-dimensional (2D) ^1H MAS NMR experiments (e.g., NOESY) that utilize the ^1H - ^1H dipolar couplings can provide direct information about the ^1H - ^1H proximities, thus allowing different proton clustering schemes to be unambiguously distinguished. ^1H - ^{29}Si cross-polarization (CP) MAS NMR provides additional constraints on the nature of the OH defects from the perspective of neighboring Si. FP calculations of energies and NMR parameters can provide insights into the relative stabilities of different candidate model structures, and also greatly increase the reliability of the assignment of NMR peaks, as compared to empirical interpretations.

In this study, we applied a similar approach of combined 1D and 2D ^1H and ^{29}Si NMR measurements and FP calculation for nominally anhydrous MgSiO_3 orthoenstatite. Furthermore, we also calculated polarized

IR absorption spectra, in addition to energy and NMR parameters, from FP calculations, so that the vibrational band assignment can be placed on a firm ground.

Experimental, analytical and calculation methods

Sample synthesis and descriptions

A hydrous MgSiO_3 orthoenstatite sample was synthesized from a mixture of $\text{MgSiO}_3 + \text{Mg}(\text{OH})_2 + \text{SiO}_2$ (with a bulk composition of $\text{MgSiO}_3 + 0.1 \text{ wt}\% \text{ H}_2\text{O}$), in a sealed Pt capsule, at 7 GPa and 1200 °C for 1 h, using a 5000-ton Kawai-type double-stage uniaxial split-sphere multi-anvil press at the Institute for Planetary Materials (IPM), Okayama University.

The target pressure (7 GPa, close to the upper stability limit) and water content (0.1 wt% H_2O , close to the reported maximum solubility) have been chosen so as to have as large a water content as possible in order to make it feasible for a variety of NMR measurements, but with minimal amount of coexisting quenched fluid phases that may complicate the NMR spectral interpretation.

The sample was confirmed to consist of only orthoenstatite by micro-Raman and ^{29}Si MAS NMR, with no additional phases detected. Quantitative electron microprobe analysis (EPMA) yielded a chemical formula of $\text{Mg}_{1.002(1)}\text{Si}_{0.996(2)}\text{O}_3$, close to the ideal formula. Both IR and ^1H MAS NMR measurements confirmed that water was incorporated in the crystal structure of orthoenstatite.

Detailed descriptions on the sample synthesis, and EPMA, IR and Raman analyses can be found in the [supplementary material](#).

NMR spectroscopy

^1H and ^{29}Si NMR spectra were obtained on coarsely crushed sample under ambient conditions, at a resonance frequency of 400.4 and 79.5 MHz, respectively, using a Varian 9.4 Tesla Unity-Inova NMR spectrometer and a 1.6 mm T3 MAS NMR probe installed at IPM. The chemical shifts for both nuclei were referenced to tetramethylsilane (TMS), and were reproducible to better than ± 0.1 ppm.

^1H static and MAS NMR (at spinning rates of 10–30 kHz), 2D ^1H NOESY and double-quantum (DQ) MAS NMR, ^{29}Si MAS NMR, and ^1H - ^{29}Si CP MAS NMR spectra (with contact times of 2–16 ms) were obtained, as described in the [supplementary material](#).

First-principles calculations

FP density functional theory (DFT) calculations of energy, and NMR and vibrational spectroscopic parameters were performed on model structures fully optimized at 1 bar using the Quantum-ESPRESSO (QE) package (version 7.0) (Giannozzi et al. 2017; Giannozzi et al. 2009). Selected models were also examined at high pressure by structural optimization at pressures up to 8 GPa.

For OH-bearing orthoenstatite, model structures of $1 \times 1 \times 2$ supercell of MgSiO_3 orthoenstatite (containing 32 formulae and 160 atoms) with one Si in a SiA or SiB site replaced by four H atoms ($(4\text{H})_{\text{SiA}}$, $(4\text{H})_{\text{SiB}}$), or one Mg in an M1 or M2 site replaced by two H atoms ($(2\text{H})_{\text{M1}}$, $(2\text{H})_{\text{M2}}$) were investigated. This corresponds to 0.56 wt% H_2O for the $(2\text{H})_{\text{Mg}}$ models, and 1.13 wt% H_2O for the $(4\text{H})_{\text{Si}}$ models, respectively. Although the water contents are higher than the reported water solubility of MgSiO_3 orthoenstatite ($< 0.1 \text{ wt}\%$), the supercell is large enough so that the defects are isolated from one another, and thus should be reasonable for representing the local structural environments of low concentrations of OH defects.

NMR chemical shielding tensors were calculated using the Gauge-Including Projector-Augmented Wave (GIPAW) method (Pickard and Mauri 2001) implemented in the QE-GIPAW package (version 7.0), similar to our previous studies for hydrous forsterite (Xue et al. 2017b) and ussingite (Xue and Kanzaki 2024). The calculated ^1H and ^{29}Si chemical shifts are reported using brucite (space group $P-3m1$) (0.0 ppm with respect to tetramethylsilane (TMS), Xue and Kanzaki (2009) and the average of the two Si sites in defect-free MgSiO_3 orthoenstatite (SiA: -83.2 ppm; SiB: -80.7 ppm with respect to tetramethylsilane (TMS): data from this study; also see Ashbrook et al. (2007), respectively, as a secondary chemical shift standard.

Vibrational frequency and polarized IR intensities were calculated based on the density functional perturbation theory (DFPT) and within the harmonic approximation using the Phonon code of the QE package (see [supplementary material](#) for details).

Both the PBEsol and PBE functionals within the generalized gradient approximation (GGA) for the exchange-correlation energy (Perdew et al. 1996, 2008), and PAW-type pseudopotentials from the PSLibrary (Dal Corso 2014) (see supplementary material for details S4) were used. Our previous studies for similar calculations using the PBEsol functional on several silicate minerals showed that the experimental ^{29}Si and ^1H isotropic chemical shifts (δ_i^{Si} , δ_i^{H}) were reproduced within ± 2 and ± 1 ppm or better for tetrahedral Si and OH, respectively, with the agreement in relative difference generally better for local structures of greater similarity (Xue and

Kanzaki 2024; Xue et al. 2017b). The calculated δ_i^{Si} and δ_i^{H} using the two functionals are generally within about 1 ppm of each other, often with somewhat larger δ_i^{H} values for the PBEsol functional.

The calculated OH stretching frequencies using the PBEsol functional tend to be lower than those using the PBE functional. The experimentally observed frequencies mostly lie in between the two sets of values, and are closer to those of the PBE functional for moderate to strong hydrogen bonding (see supplementary Fig. 21s).

Simulation of NMR and IR spectra from FP calculation results

Simulated ^1H static and MAS NMR spectra were produced using the SIMPSON program (ver. 4.2.1)(Bak et al. 2000; Juhl et al. 2020), by considering the full chemical shift tensors and dipolar interactions among all protons, based on the geometries and NMR parameters from the FP calculation, similar to our previous study on hydrous forsterite (Xue et al. 2017b). Simulated ^{29}Si MAS and ^1H - ^{29}Si CP MAS NMR spectra were generated using the calculated δ_i^{Si} and Si-H distance information. Simulated IR absorption spectra were generated using the calculated frequencies and IR intensities, with an arbitrary Lorentzian line broadening function applied. Details can be found in the [supplementary material](#).

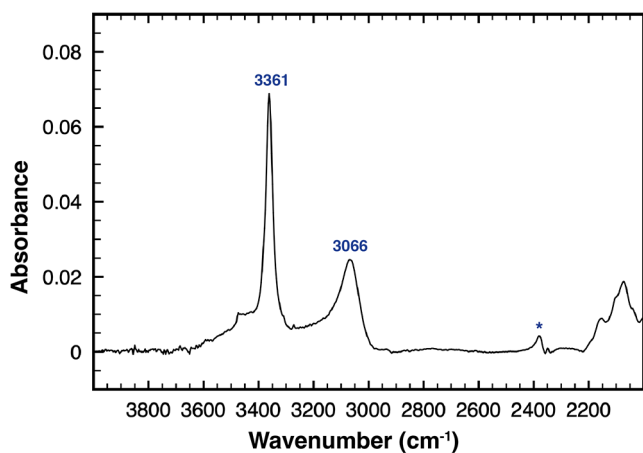


Fig. 1 Unpolarized IR absorption spectrum for a hydrous MgSiO_3 orthoenstatite sample synthesized at 7 GPa and 1200 °C. A cubic spline baseline correction has been applied. The absorbance was not normalized to sample thickness. The small features in the region of 2300–2500 cm^{-1} (marked by an asterisk) are due to imperfect subtraction of the signal from atmospheric CO_2 between the sample and the reference, and the bands below 2200 cm^{-1} are consistent with those reported for overtones of lattice vibrations for orthoenstatite (cf., Prechtel and Stalder 2012)

Results

Infrared absorption spectra

A unpolarized IR absorption spectrum of the hydrous orthoenstatite sample synthesized at 7 GPa and 1200 °C is shown in Fig. 1 (after baseline correction) and supplementary Fig. 2s (without baseline correction). The spectrum exhibits two main bands near 3361 and 3066 cm^{-1} , consistent with the A3 and A4 bands reported previously for orthoenstatite (Prechtel and Stalder 2010, 2011). No bands near 3687 and 3592 cm^{-1} , corresponding to the A1 and A2 bands previously reported, are detected. No bands other than those due to atmospheric CO_2 and overtones of lattice vibrations are recognized below 3000 cm^{-1} .

^1H MAS and static NMR spectra, and 2D NOESY and DQ MAS NMR spectra

The fully-relaxed ^1H MAS NMR spectra of the hydrous orthoenstatite sample from this study, acquired at a spinning rate of 30 kHz and a sufficiently long relaxation delay (d1) of 100 s, and that with a short d1 of 3 s (both after rotor background subtraction) are shown in Fig. 2b and 2a, respectively. Both spectra contain two narrow peaks near 7.6 and 5.9 ppm, with a full width at half maximum (FWHM) of 0.25 and 0.24 ppm and nearly symmetric Lorentzian peak shape (with slight tails on the outside of the doublet). In addition, there is a weak broader peak with a maximum near 4.9 ppm (shown in Fig. 2c) that has a much shorter ^1H T_1 (~1 s) than those of the two narrow peaks (15–17 s), so that it disappears in the difference spectrum between the two spectra (see Fig. 2d). It is well known that low concentrations of water in silicate minerals and glasses tend to have much longer ^1H T_1 than those in nominally hydrous phases or surface adsorbed water, due to the lack of efficient relaxation mechanisms (e.g., Xue and Kanzaki 2004; Xue et al. 2006, 2017b). Thus, the two narrow peaks near 7.6 and 5.9 ppm may be attributed to low concentrations of protons incorporated in the orthoenstatite structure (Table 1). The weak, broader peak near 4.9 ppm may be due to protons in quenched fluids/melts at grain boundaries.

The total H_2O content of the sample was estimated from the total intensity (including the broad component) of the fully relaxed ^1H MAS NMR spectra to be 0.11(1) wt%, close to the nominal value (0.1 wt%). The total H_2O content for water incorporated in the crystal structure of orthoenstatite, estimated from the total intensities of the two narrow peaks, is 0.05(1) wt%.

An earlier study by Kohn (1996) also reported two small narrow peaks near 7.9 and 5.9 ppm, along with several other narrow and broad peaks, in the ^1H MAS NMR spectrum

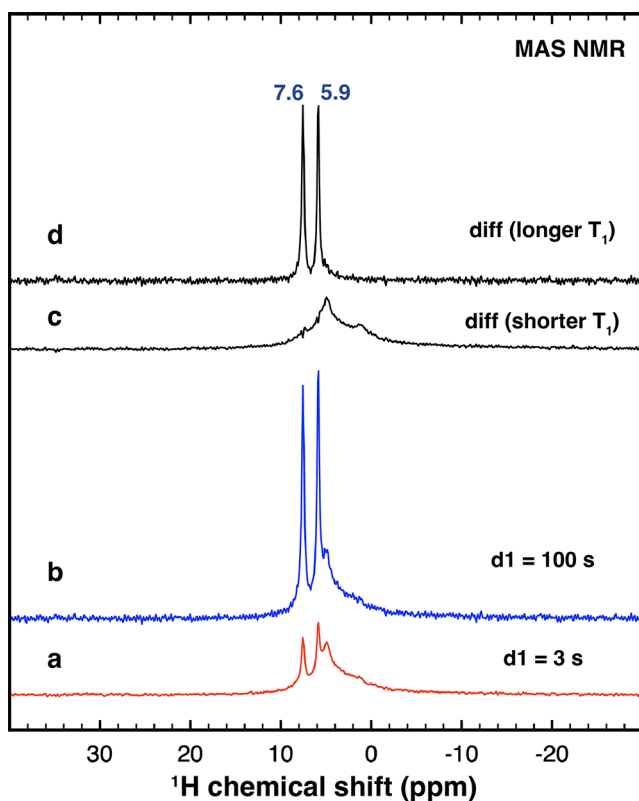


Fig. 2 ^1H MAS NMR spectra of a hydrous MgSiO_3 orthoenstatite sample synthesized at 7 GPa and 1200 °C at a spinning rate of 30 kHz and a recycle delay (d1) of 3 s (a) and 100 s (b), difference spectrum between (b) and (a) for the components of longer T_1 (d), and the spectrum of the component with a short T_1 obtained by subtracting the spectrum of (d), scaled by an intensity factor, from that of (a) to eliminate the narrow peaks (c). A Lorentzian line broadening function of 20 Hz has been applied to (a) and (b). All spectra have been plotted with a common intensity scale

of an MgSiO_3 orthoenstatite sample synthesized at 1.5 GPa and 1000–1150 °C under water saturated condition. These two peaks likely correspond to those from the present study. They were less prominent with respect to the broad peak, possibly because of lower water solubility at lower pressure, coupled with more excess water in their starting material (> 1 wt% H_2O added).

From here on, we will only present ^1H NMR spectra that represent the difference between the two spectra acquired at a d1 of 100 s and 3 s, and discuss in terms of protons incorporated in the orthoenstatite structure.

The ^1H MAS NMR spectra acquired at spinning rates of 10, 20 and 30 kHz for the orthoenstatite sample from this study are compared in Fig. 3a. The widths of the two peaks increase, and their peak shapes become increasingly asymmetric, at lower spinning rates. A similar phenomenon has been observed for dense hydrous magnesium silicates, phase B and superhydrous B, in which a pair of dissimilar protons are in close proximity (Phillips et al. 1997). The asymmetric

Table 1 ^1H and ^{29}Si NMR parameters for a hydrous MgSiO_3 orthoenstatite sample synthesized at 7 GPa and 1200 °C

Peak	δ_i (ppm)	FWHM (ppm) ^a	Assignment
^1H MAS NMR:			
Peak 1	7.6	0.25	O2a-H···O1a
Peak 2	5.9	0.24	O2b-H···O1b
^{29}Si MAS NMR:			
Peak 1	-80.7	0.37	SiB
Peak 2	-83.2	0.35	SiA
^1H - ^{29}Si CP MAS NMR:			
Peak 1	-79.2	0.53	SiB adjacent to $(2\text{H})_{\text{M}2}$ defects & bonded to O1b···H
Peak 2	-80.6	0.59	SiA adjacent to $(2\text{H})_{\text{M}2}$ defects & bonded to O1a···H
Peak 3	-81.0	0.49	SiB adjacent to $(2\text{H})_{\text{M}2}$ defects & bonded to O2b-H
Peak 4	-82.7	0.41	
Peak 5	-83.3	0.50	
Peak 6	-84.1	0.57	
Peak 7	-85.5	0.43	SiA adjacent to $(2\text{H})_{\text{M}2}$ defects & bonded to O2a-H

^a Full width at half maximum (FWHM) excluding contribution from any applied line broadening. FWHM for the ^1H MAS NMR correspond to those at a spinning rate of 30 kHz, and those for the ^{29}Si MAS and ^1H - ^{29}Si CP MAS NMR at 20 kHz

peak shape of the doublet is caused by combined chemical shift anisotropy and dipolar interaction between the two protons.

The ^1H static NMR spectrum of the sample spans a chemical shift range of about 80 ppm (see Fig. 4a), which is narrower than our previously reported spectra (spanning a range of about 200 ppm) for hydrous forsterite and katoite that both show the $(4\text{H})_{\text{Si}}$ substitution (Xue et al. 2017b).

Information about the relative proximities among the protons can be obtained from 2D ^1H NOESY and DQ MAS NMR. The 2D ^1H NOESY spectra of the sample show clear cross peaks between the two peaks near 7.6 and 5.9 ppm, with the relative intensity of the cross peak/diagonal peak increasing with mixing time (see Fig. 5a for the spectrum with a mixing time of 5 s). The 2D ^1H DQ MAS NMR spectrum exhibits a pair of cross peaks between the two peaks, but no diagonal peaks (see Fig. 5b). Both types of spectra indicate that the two distinct proton sites are in spatial proximity. Note that the DQ NMR experiment differs from the NOESY in that a diagonal peak in the former is an indication of close proximity between a pair of spins of identical chemical shift, whereas diagonal peaks are always present in the latter. The lack of diagonal peaks in the 2D ^1H DQ MAS NMR spectrum suggests that protons in the same site are remote from one another. Thus, the protons are incorporated in the crystal structure as a pair of dissimilar protons that are relatively close to each other, with different proton pairs remote from one another.

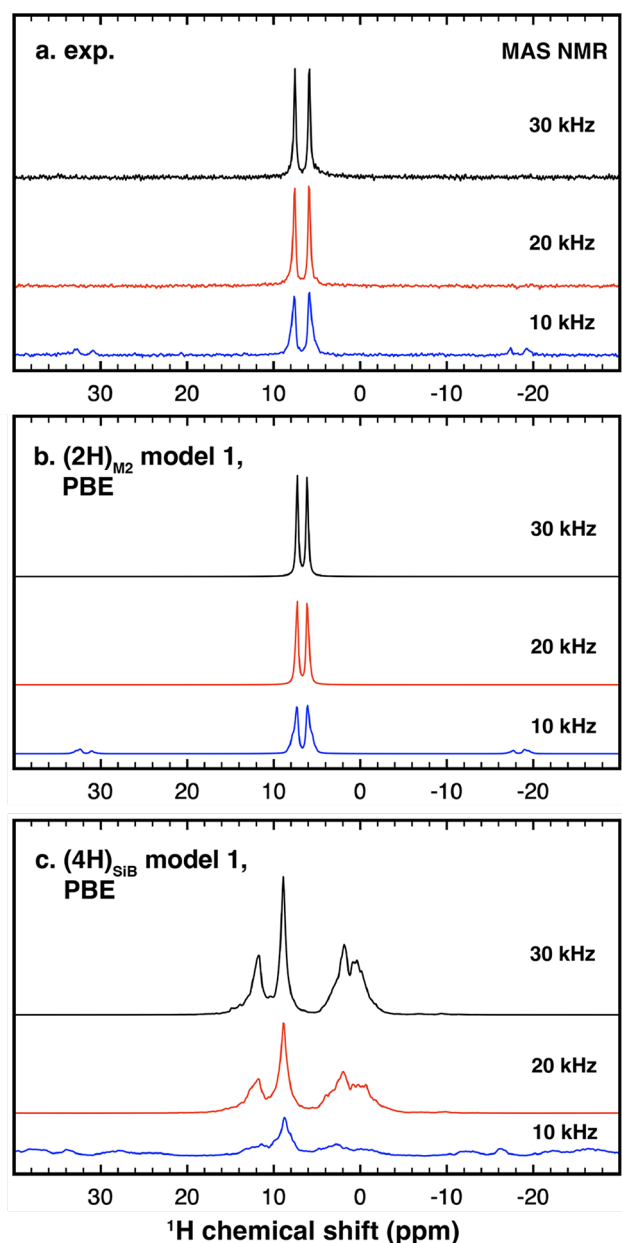


Fig. 3 ^1H MAS NMR spectra (difference spectra between that at a recycle delay of 100 s and 3 s) of a hydrous MgSiO_3 orthoenstatite sample synthesized at 7 GPa and 1200 °C at a spinning rate of 10, 20 and 30 kHz (bottom to top as labeled) (a), and ^1H MAS NMR spectra at a spinning rate of 10, 20 and 30 kHz (bottom to top as labeled) simulated with the SIMPSON program for the $(2\text{H})_{\text{M}_2}$ model 1 (b) and $(4\text{H})_{\text{SiB}}$ model 1 (c) of MgSiO_3 orthoenstatite from FP calculation at 1 bar using the PBE functional. A Lorentzian line broadening function of 20 Hz has been applied to (a), and 100 Hz used for (b) and (c). The spectra at different spinning rates within each of (a)–(c) have been plotted with a common intensity scale

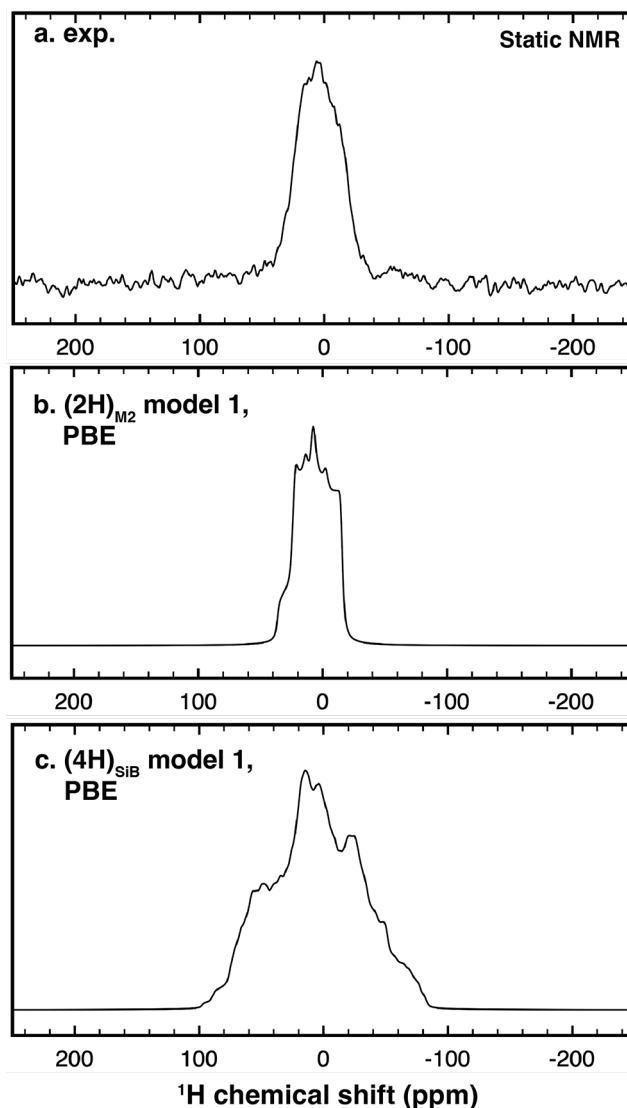


Fig. 4 ^1H static NMR spectrum (difference spectrum between that at a recycle delay of 100 s and 3 s) of a hydrous MgSiO_3 orthoenstatite sample synthesized at 7 GPa and 1200 °C (a), and ^1H static NMR spectrum simulated with the SIMPSON program for the $(2\text{H})_{\text{M}_2}$ model 1 (b) and $(4\text{H})_{\text{SiB}}$ model 1 (c) of MgSiO_3 orthoenstatite from FP calculation at 1 bar using the PBE functional. A Lorentzian line broadening function of 1000 Hz has been used for all

^{29}Si MAS and ^1H - ^{29}Si CP MAS NMR spectra

The ^{29}Si MAS NMR spectrum of the hydrous orthoenstatite sample from this study contains two narrow peaks near -80.7 and -83.2 ppm (see Fig. 6a; Table 1). These peaks match well with those reported previously for orthoenstatite (Ashbrook et al. 2007), and show a small difference in peak position from those of low-pressure clinoenstatite (-80.5 and -83.1 ppm) synthesized at ambient pressure from our previous study (Kanzaki and Xue 2017). No other peaks were observed.

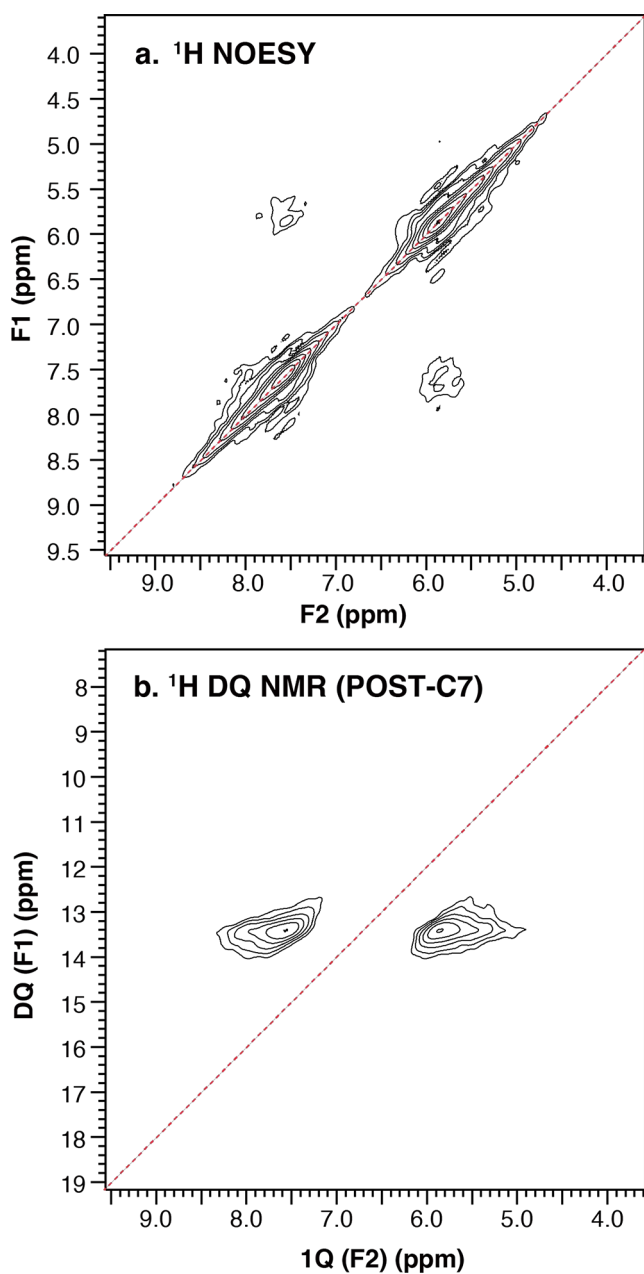


Fig. 5 2D ^1H NOESY (with a mixing time of 5 s) (a) and DQ MAS NMR spectrum (with a DQ excitation/reconversion duration of 144 μs each) (b) of a hydrous MgSiO_3 orthoenstatite sample synthesized at 7 GPa and 1200 $^\circ\text{C}$ at a spinning rate of 10 kHz. A Lorentzian line broadening function of 20 Hz has been applied to both dimensions. The red diagonal dashed line is a guide for diagonal peaks

The ^1H - ^{29}Si CP MAS NMR spectra of the sample with contact times of 2–16 ms show four groups of peaks near -79.2 , -80.9 , -83.3 and -85.5 ppm (see Fig. 6). The peak near -80.9 ppm has a left shoulder, and the peak around -83.3 ppm likely represents several partially overlapping peaks. Curve fitting using Lorentzian peaks were performed, which gave seven components with FWHM of 0.41–0.59 ppm (see Table 1 and supplementary Fig. 3s). These peaks

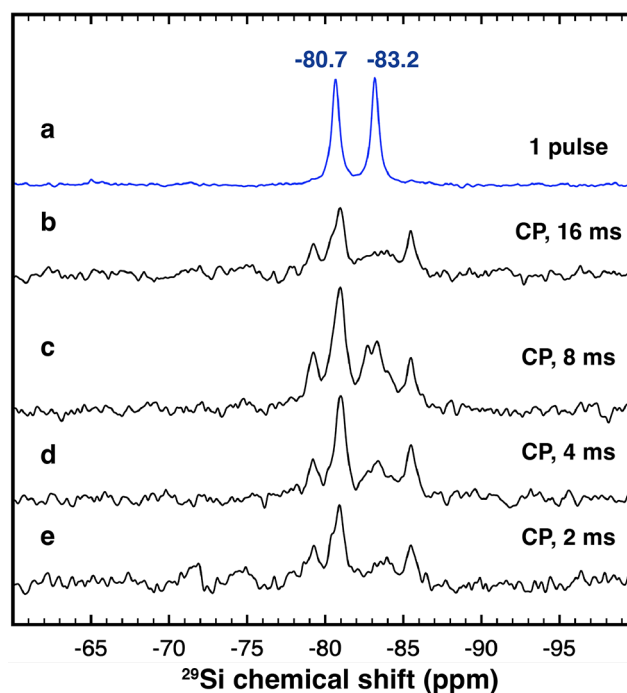


Fig. 6 ^{29}Si MAS NMR spectrum obtained with a 45° pulse and a recycle delay of 1000 s (a), and ^1H - ^{29}Si CP MAS NMR spectra at a contact time of 16, 8, 4 and 2 ms (b to e) and a recycle delay of 20 s, all at a spinning rate of 20 kHz, for a hydrous MgSiO_3 orthoenstatite sample synthesized at 7 GPa and 1200 $^\circ\text{C}$. A Lorentzian line broadening function of 20 Hz has been applied to all. All the CP spectra have been plotted with a common intensity scale

cannot be attributed to any known hydrous Mg silicate phases that may be stable under the synthesis condition, and thus must represent Si sites that are in the vicinity of protons in orthoenstatite. They provide further constraints on the water incorporation mechanisms.

First-principles calculation

Geometries and energies

The energy and cell volume for all the models are shown in Table 2. The energetically most favorable models for the $(2\text{H})_{\text{Mg}}$ and $(4\text{H})_{\text{Si}}$ defects, i.e., the $(2\text{H})_{\text{M}2}$ model 1 and $(4\text{H})_{\text{SiB}}$ model 1, calculated using the PBEsol functional, are shown in Fig. 7. The configurations optimized using the PBE functional are similar. The crystal structure data for both models, as well as those of brucite and defect-free MgSiO_3 orthoenstatite, optimized using both functionals, can be found in the [supplementary material](#).

$(2\text{H})_{\text{M}1}$ and $(2\text{H})_{\text{M}2}$ models

In the orthoenstatite structure, each Mg in the M1 site is bonded to one O2a and two O1a atoms on one octahedral

Table 2 Energy (E) and cell volume (V) for different MgSiO₃ orthoenstatite models from FP calculation at 1 bar using the PBEsol and PBE functionals

Model	E,PBEsol (Ry)	ΔE,PBEsol (Ry) ^a	ΔE,PBEsol (eV) ^a	ΔE,PBEsol (kJ/mol) ^a	V,PBEsol (Å ³)	V,PBE (Å ³)
Defect-free orthoenstatite	-6479.0775				1669.624	1728.542
(2H) _{Mg} models:						
(2H) _{M2} model 1	-6448.4387	0.0000	0.000	0.00	1673.929	1736.928
(2H) _{M1} model 1	-6448.3817	0.0570	0.776	74.85	1672.258	
(4H) _{Si} models:						
(4H) _{SiB} model 1	-6437.8538	0.0000	0.000	0.00	1674.603	1732.180
(4H) _{SiB} model 2	-6437.8437	0.0101	0.137	13.23	1673.766	
(4H) _{SiB} model 3	-6437.8433	0.0105	0.143	13.80	1676.817	
(4H) _{SiB} model 4	-6437.8419	0.0118	0.161	15.55	1674.821	
(4H) _{SiB} model 5	-6437.8273	0.0265	0.361	34.80	1670.525	
(4H) _{SiB} model 6	-6437.8185	0.0353	0.481	46.37	1675.632	
(4H) _{SiA} model 1	-6437.8229	0.0308	0.420	40.50	1670.926	
(4H) _{SiA} model 2	-6437.8184	0.0354	0.481	46.45	1673.476	
(4H) _{SiA} model 3	-6437.8117	0.0421	0.573	55.28	1673.809	

Note all values refer to that of 1 × 1 × 2 supercell

^aΔE refers to energy difference with respect to the lowest-energy model of the same composition (i.e., (2H)_{M2} model 1 or (4H)_{SiB} model 1)

face, and to one O2b and two O1b atoms on the opposite face, both parallel to the (001) plane; whereas each Mg in the M2 site is bonded to one O2a, one O1a and one O3a on one octahedral face, and to one O2b, one O1b and one O3b on the opposite face, both parallel to the (001) plane (see supplementary Fig. 4s). The O1a and O1b are apical nonbridging oxygen atoms, O2a and O2b are equatorial nonbridging oxygen atoms, and O3a and O3b are bridging oxygen atoms on the SiO₄ tetrahedra of SiA and SiB, respectively.

The two H atoms in both the (2H)_{M2} model 1 and (2H)_{M1} model 1 form O2a-H1···O1a and O2b-H2···O1b linkages within the (001) plane (see Fig. 7a and supplementary Fig. 4s), similar to that reported by Balan et al. (2013). The hydrogen bonding for both linkages are relatively strong, with that of the O2a-H1···O1a linkage stronger. Note that the two OH groups are each bonded to a Si, similar to that of (2H)_{Mg} defects in olivine (Xue et al. 2017b).

The configurations for both models were found to remain unchanged at 7 GPa using the PBEsol functional. The (2H)_{M2} model 1 is significantly lower in enthalpy than the (2H)_{M1} model 1, by 75 kJ/mol at 1 bar (see Table 2) and 70 kJ/mol at 7 GPa. Thus, the (2H)_{M2} model 1 is the more plausible incorporation mechanism for the (2H)_{Mg} defects in orthoenstatite, and the (2H)_{M1} defects are expected to be negligible.

(4H)_{SiA} and (4H)_{SiB} models

The two types of silicate chains of SiA and SiB are located in alternating silicate layers along the *a* axis. Each SiA is bonded to one O2a, one O1a and two O3a atoms, and each SiB is bonded to one O2b, one O1b and two O3b atoms.

Whereas for the SiB tetrahedra, oxygen is shared with neighboring MgO₆ octahedra only by corners, for the SiA tetrahedra, one O2a-O3a edge is shared with a neighboring M2 octahedron. The two O3a (O3b) atoms on each vacant tetrahedron in the (4H)_{SiA} and (4H)_{SiB} models are not equivalent. For the (4H)_{SiA} models, one O3a is edge-sharing and another is corner sharing. For the (4H)_{SiB} models, the two O3b's have inequivalent O3b-O2b distances. These differences render the O-H bonds attached to the two O3a (O3b) atoms inequivalent.

Six model structures for the (4H)_{SiB} defects, and three for the (4H)_{SiA} defects, with different configurations of the 4H, were found at 1 bar using the PBEsol functional, and are labelled model 1 to 6 (3) in the order of increasing energy (see supplementary Fig. 5s, 6s and Table 2). Compared with the lowest-energy (4H)_{SiB} model 1, the (4H)_{SiB} models 2 to 6 are 13 to 46 kJ/mol higher in energy, and the (4H)_{SiA} models are 41 to 55 kJ/mol higher at 1 bar (see Table 2). Note that our (4H)_{SiB} model 4 resembles the (4H)_{SiB} model reported by Balan et al. (2013) and the Conf.Si-1 model by Sakurai et al. (2014), our (4H)_{SiB} model 3 resembles the Conf. Si-2 model of Sakurai et al. (2014), and our (4H)_{SiA} model 3 resembles the (4H)_{SiA} model reported by Balan et al. (2013), which are thus all not the most favorable configurations.

The configurations for all the (4H)_{SiB} and (4H)_{SiA} models investigated, except for the (4H)_{SiB} models 2 and 4, were found to remain unchanged at high pressure using the PBEsol functional. The (4H)_{SiB} model 1 remains the energetically most favorable among all up to 8 GPa (see supplementary Fig. 7s and Table 1s), and thus the most plausible configuration for the (4H)_{Si} defects in orthoenstatite.

In the (4H)_{SiB} model 1, the four H atoms (labelled H1 to H4) are each bonded to one of the oxygen atoms on the

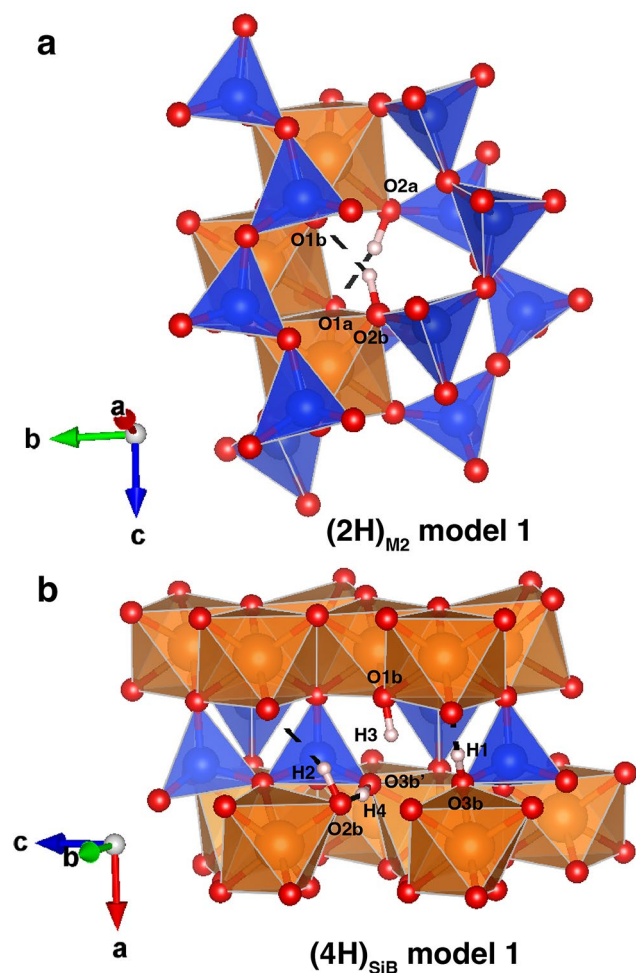


Fig. 7 The energetically most favorable $(2H)_{M2}$ model 1 (a) and $(4H)_{SiB}$ model 1 of $MgSiO_3$ orthoenstatite from FP calculation at 1 bar using the PBEsol functional, which have similar configurations as those calculated using the PBE functional. Blue tetrahedra and orange octahedra represent SiO_4 tetrahedra and MgO_6 octahedra, respectively. Blue, orange, red and pink spheres represent Si, Mg, O and H atoms, respectively. Only part of the structure around the respective Mg or Si vacancy is shown for clarity. Drawn using the Vesta program (Momma and Izumi 2011)

vacant tetrahedron: the H1 on one of O3b (that has a longer O3b-O2b distance before relaxation) is pointing away from the vacant tetrahedron and located in the same silicate layer, forming a moderately strong hydrogen bond with an O2b on a different (occupied) tetrahedron; the H4 on another O3b, which will be referred to as O3b' from hereafter, forms strong hydrogen bonding with the O2b on the vacant tetrahedron; the H2 on O2b is also pointing away from the vacant tetrahedron and located in the same silicate layer, but does not form significant hydrogen bonding; the H3 on O1b is pointing toward the center of the vacant tetrahedron with little hydrogen bonding (see Fig. 7b, supplementary Fig. 5s and Table 3).

The geometries for the other $(4H)_{SiB}$ and $(4H)_{SiA}$ models and their high-pressure behaviors are described in detail in the [supplementary material](#). A prominent difference between the different models lies in the orientation of one of the two O3-H bonds (O3b-H1, O3a-H3), with the O3-H pointing away from the vacant tetrahedron forming stronger hydrogen bonding in the $(4H)_{SiB}$ model 1 and $(4H)_{SiA}$ model 2, but inside the vacant tetrahedron in the higher-energy models (see supplementary Fig. 5s and 6s).

It is also worth mentioning that the $(4H)_{SiA}$ model 1 and $(4H)_{SiB}$ model HP-2 (obtained after relaxing $(4H)_{SiB}$ model 2 at 6–8 GPa) both have a unique 4H configuration, in which there are two H atoms on O2, but no H on one of the O3 atoms (O3b', O3a') of the vacant tetrahedron (see supplementary Fig. 6s and 8s). In a sense, the configuration of two H atoms on O2 resembles molecular H_2O . Although these models are energetically unfavorable for orthoenstatite, such a configuration could be important in other high-pressure minerals.

There is a general trend of stronger hydrogen bonding for a proton bonded to a bridging oxygen (O3) atom, than that bonded to a nonbridging oxygen (O2, O1) atom, in all the $(4H)_{SiB}$ and $(4H)_{SiA}$ models. The former results in a SiOH linkage, similar to those in the $(2H)_{Mg}$ defects, whereas the latter results in an OH linked to no Si. Note that strictly speaking, the O3 on a Si vacancy becomes a nonbridging oxygen atom (bonded to only one Si), and the O1 and O2 become free oxygen atoms (hydroxyls) (bonded to no Si). Nevertheless, we will continue to refer to them as bridging oxygen/nonbridging oxygen in terms of the defect-free structure throughout. The trend in hydrogen bonding can be well explained by the bond valence model (cf., Brown 2002). The bond valence is defined to be a function of bond distance (e.g., $S_{ij} = \exp((R_0 - R_{ij})/B)$, where S_{ij} and R_{ij} are the bond valence and bond distance between atom i and j , and R_0 and B are constant parameters). The valence sum rule of the bond valence model requires the bond valence sum around any ion to be equal to the valence of the ion to ensure local charge neutrality (cf., Brown 2002). The bond valence sum around O3 in a SiOH linkage is larger than that around O1/O2 in a OH group bonded to no Si. Therefore, the former should favor longer O-H bond (stronger hydrogen bonding). It is commonly known from mineral structures that OH groups bonded to a high field strength cation like Si, such as those in pectolite ($NaCa_2Si_3O_8OH$) and ussingite ($Na_2AlSi_3O_8OH$), tend to yield strong hydrogen bonding, whereas those only bonded to low-field strength cations (e.g., Mg, Ca), such as those in brucite and many lower-pressure hydrous magnesium silicate minerals (e.g., amphibole, chondrodite, phase A), tend to give weak or no hydrogen bonding (cf., Xue and Kanzaki 2004).

Table 3 ^1H isotropic chemical shift (δ_i^{H}) and O-H, $\text{H}\cdots\text{O}$ and $\text{O}\cdots\text{O}$ distances and O-H \cdots O angle for the energetically most favorable defect models of MgSiO_3 orthoenstatite from FP calculation at 1 bar using the PBEsol and PBE functionals

H site ^a	Functional	δ_i^{H} (ppm)	R(O-H) (Å)	R(H \cdots O) (Å) ^b	R(O \cdots O) (Å) ^b	$\angle\text{O-H}\cdots\text{O}$ ($^\circ$) ^b	Linkage ^b
(2H) _{M2} model 1							
H1	PBEsol	7.96	1.016	1.73	2.715	161.99	O2a-H2 \cdots O1a
(161)	PBE	7.23	1.001	1.858	2.822	160.79	O2a-H2 \cdots O1a
H2	PBEsol	5.89	0.997	2.004	2.920	151.58	O2b-H1 \cdots O1b
(160)	PBE	6.16	0.990	2.035	2.949	152.50	O2b-H1 \cdots O1b
(4H) _{SiB} model 1							
H1	PBEsol	9.28	1.025	1.577	2.601	177.74	O3b-H1 \cdots O2b (different tetrahedron)
(160)	PBE	8.94	1.010	1.644	2.652	175.68	O3b-H1 \cdots O2b (different tetrahedron)
H2	PBEsol	1.24	0.984	2.077	3.010	157.62	O2b-H2 \cdots O2b (different tetrahedron)
(161)	PBE	1.02	0.975	2.200	3.108	154.23	O2b-H2 \cdots O2b (different tetrahedron)
H3	PBEsol	1.09	0.973	2.227	2.940	129.11	O1b-H3 \cdots O2b
(162)	PBE	1.62	0.969	2.304	3.031	131.15	O1b-H3 \cdots O2b
H4	PBEsol	12.68	1.059	1.478	2.522	167.41	O3b'-H4 \cdots O2b
(163)	PBE	11.57	1.030	1.577	2.594	168.26	O3b'-H4 \cdots O2b

Note δ_i^{H} is calculated from the isotropic chemical shielding (σ_i^{H}) as the following: δ_i^{H} (ppm) = σ_i^{H} , ref + δ_i^{H} , ref - σ_i^{H} , ref (ppm), where σ_i^{H} , ref (29.30 ppm for the PBEsol, and 30.79 ppm for the PBE functional) and δ_i^{H} , ref (0.0 ppm: Xue and Kanzaki 2009) are the values for brucite

^a Numbers in brackets are the site numbers in the crystal structure data included in the supplementary material

^b For OH with long H \cdots O distances, more than one O-H \cdots O linkages often exist. Only the one with the shortest H \cdots O distance and largest O-H \cdots O angle is listed. O-H \cdots O linkages with H \cdots O distances > 2 Å often have small O-H \cdots O angles, and likely do not represent significant hydrogen-bonding interaction

The greater stability of the (4H)_{SiB} model 1, which yields stronger hydrogen bonding for the O3b-H1 \cdots O linkage than the other (4H)_{SiB} models with different orientations of the O3b-H1, can also be well explained by the bond valence model. The O3b (in the Si-O3b-H1 \cdots O linkage) should favor longer O-H bond (stronger hydrogen bonding) in order to better achieve local charge neutrality, because of larger bond valence sum as compared to the those of O1b/O2b (with the OH linked to no Si). The hydrogen bonding for the O3b'-H (in the Si-O3b'-H4 \cdots O2b linkage) exhibits less variations among the (4H)_{SiB} models, because of similar configurations and already very strong hydrogen bonding.

^1H NMR results

The ^1H isotropic chemical shifts, δ_i^{H} , and the corresponding hydrogen bonding (O-H, H \cdots O and O \cdots O) distances and O-H \cdots O angles for the energetically most favorable (2H)_{M2} model 1 and (4H)_{SiB} model 1, calculated using both the PBE and PBEsol functionals, are tabulated in Table 3. Those for the other models calculated using the PBEsol functional can be found in supplementary Table 2s.

(2H)_{M1} and (2H)_{M2} models

The (2H)_{M2} model 1 yields two protons with δ_i^{H} of 7.2 and 6.2 ppm using the PBE functional, and 8.0 and 5.9 ppm using the PBEsol functional. Both are in reasonable agreement with the experimentally observed peaks at 7.6 and 5.9 ppm for the hydrous orthoenstatite sample from this study.

These two δ_i^{H} values correspond to the O2a-H2 \cdots O1a and O2b-H1 \cdots O1b linkage, respectively.

The simulated ^1H MAS NMR spectra at spinning rates of 10, 20 and 30 kHz for the (2H)_{M2} model 1 calculated using the two functionals are compared with the corresponding experimental NMR spectra for the hydrous orthoenstatite sample from this study in Fig. 3 and supplementary Fig. 9s. Both the peak width and the asymmetric peak shape of the experimental NMR spectra are well reproduced at each spinning rate (including the asymmetric shape of the spinning sidebands at 10 kHz) with either functional.

The simulated ^1H static MAS spectra for the (2H)_{M2} model 1 calculated using the two functionals also both reasonably reproduced the range of chemical shift and peak shape of the experimental spectrum for the sample from this study (see Fig. 4 and supplementary Fig. 11s).

On the other hand, the (2H)_{M1} model 1 predicts broader ^1H MAS peak widths, and broader and more complicated ^1H static NMR peak shape than observed (see supplementary Fig. 10s and 12s), due to the smaller size and accordingly shorter H-H distance for the M1 site.

Thus, overall the (2H)_{M2} model 1 well reproduced the ^1H MAS and static NMR spectra for the hydrous orthoenstatite sample from this study. Together with the 2D ^1H NOESY and DQ MAS NMR results that indicate the two proton sites form a spatially close pair, and the much lower calculated energy of the (2H)_{M2} model 1 than (2H)_{M1} model 1, it is beyond any doubts that the observed ^1H NMR peaks at 7.6 and 5.9 ppm are due to protons associated with M2 vacancies with a configuration of (2H)_{M2} model 1.

(4H)_{SiA} and (4H)_{SiB} models

The (4H)_{SiB} model 1 predicts four ¹H MAS NMR peaks near 1.6, 1.0, 8.9 and 11.6 ppm using the PBE functional, and near 1.1, 1.2, 9.3 and 12.7 ppm using the PBEsol functional (see Table 3). The proton with the largest δ_i^H (11.6/12.7 ppm) corresponds to the H (H4) bonded to the O3b' (bridging oxygen), which forms strong hydrogen bond with the O2 on the vacant tetrahedron, and the one with the second largest δ_i^H (8.9/9.3 ppm) corresponds to the H (H1) bonded to the other bridging oxygen, O3b, and pointing away from the vacant tetrahedron toward an O2b on a different (occupied) tetrahedron. The two protons with small δ_i^H (H3: 1.6/1.1 ppm, H2: 1.0/1.2 ppm) correspond to those bonded to the O1b and O2b (both nonbridging oxygen atoms), respectively (see Table 3). Note that the two δ_i^H values separated by a slash correspond to those calculated using the PBE/PBEsol functional.

The δ_i^H exhibits a general correlation with the hydrogen-bonding O-H, H \cdots O, and O \cdots O distances (see supplementary Fig. 13s), as has been known experimentally (cf., Xue and Kanzaki 2009).

The predicted δ_i^H for the higher-energy (4H)_{SiB} models 2 and 4 at 1 bar, calculated using the PBEsol functional, also each show four peaks that span a range of δ_i^H values from large (12–14 ppm) to small (~1 ppm), with the largest variation among the different (4H)_{SiB} models on the second largest δ_i^H for the H1 on the O3b, because of the different O3b-H1 orientations for the different models (see supplementary Table 2s). Similarly, the predicted δ_i^H for the higher-energy (4H)_{SiA} models 1, 2 and 3, using the PBEsol functional, also each show four peaks that span a range of δ_i^H from large to small, again with the largest variation among the different (4H)_{SiA} models on the second largest δ_i^H for the H (H3) on one of the bridging oxygens, O3a, because of different O3a-H3 orientations for the different models (see supplementary Table 2s).

The simulated ¹H MAS NMR spectra (at spinning rates of 10, 20 and 30 kHz) for the (4H)_{SiB} model 1 using the PBE and PBEsol functionals are overall similar (see Fig. 3c and supplementary Fig. 14s). They contain four ¹H peaks ranging from about 1 to 12 ppm, with varying peak widths that are overall broader than those of the (2H)_{M2} model 1, due to stronger ¹H-¹H homonuclear dipolar interactions within the 4H cluster. The two narrower, more resolved peaks with larger δ_i^H are each dominantly due to H4 (bonded to O3b') and H1 (bonded to O3b), respectively, whereas the two broader, strongly overlapping peaks with small δ_i^H are jointly contributed by the remaining two H sites that are strongly dipolar coupled with each other.

The simulated ¹H MAS NMR spectra for the other (4H)_{SiB} and (4H)_{SiA} models (at 30 kHz only) using the

PBEsol functional also yield peaks in a similar chemical shift range (see supplementary Fig. 15s). The peak widths and peak positions, especially those of the peak with the second largest δ_i^H , however, vary largely depending on the model, because of different 4H configurations, suggesting that ¹H MAS NMR is a sensitive probe to distinguish different 4H configurations.

The simulated ¹H static spectra for the (4H)_{SiB} model 1 using the two functionals are also similar (see Fig. 4 and supplementary Fig. 16s). They span a large chemical shift range of about 200 ppm, due to strong ¹H-¹H dipolar coupling within the 4H cluster, with a narrower component (doublet) near the middle that is primarily due to the H1, which is bonded to the O3b and pointing away from the vacant tetrahedron, and thus experiences less dipolar coupling.

The simulated ¹H static NMR spectra for the other (4H)_{SiB} and (4H)_{SiA} models using the PBEsol functional show similar chemical shift ranges, with the peak shape varying depending on the model because of the different 4H configurations (see supplementary Fig. 17s). These features overall resemble, but are not identical to the ¹H static NMR spectra for the (4H)_{Si} defects of forsterite reported previously (Xue et al. 2017b).

If a hydrous orthoenstatite sample contains protons associated Si vacancies, its ¹H MAS NMR spectra are expected to resemble those shown in Fig. 3c and supplementary Fig. 14s, and its static NMR spectrum resemble those in Fig. 4c and supplementary Fig. 16s for the (4H)_{SiB} model 1. The observed spectra of the hydrous orthoenstatite sample from this study (see Figs. 3a and 4a) do not agree with the predicted spectra, consistent with the lack of protons associated with Si vacancies in the sample.

It should be mentioned in passing that comparable water incorporation mechanisms are expected for low-pressure clinoenstatite and orthoenstatite, as indicated by the overall similarity in their IR spectra in the OH stretching region (e.g., Bromiley and Bromiley 2006; Rauch and Keppler 2002; Withers and Hirschmann 2007). Our parallel study on a hydrous low-pressure clinoenstatite sample obtained after recovering high-pressure clinoenstatite synthesized at 14 GPa and 1200 °C to ambient conditions indeed revealed ¹H NMR spectra resembling those predicted for the (4H)_{SiB} model 1 of orthoenstatite, and well-reproduced by FP calculation results for (4H)_{Si} defect models of low-pressure clinoenstatite converted from high-pressure clinoenstatite (Xue et al. 2018), lending confidence to these calculation results.

²⁹Si NMR results

The FP calculation for the defect-free MgSiO₃ orthoenstatite yielded a difference in ²⁹Si isotropic chemical shift, δ_i^{Si} ,

of 2.7 and 3.8 ppm between the two Si sites (see Table 4; Fig. 8 and supplementary Fig. 18s) using the PBE and PBEsol functional, respectively, as compared to 2.5 ppm in the experimental NMR spectra (-80.7 and -83.2 ppm, see Table 1; Figs. 6 and 8). We have used the average of the two peaks for referencing the other models. The peak with a more negative δ_i^{Si} corresponds to the SiA site (see Table 4).

The simulated single-pulse ^{29}Si MAS NMR spectra for the defect-free orthoenstatite using the two functionals are shown in Fig. 8 and supplementary Fig. 18s. Considering the low water solubility (<0.1 wt% H_2O) of orthoenstatite, they may also be regarded as representing single-pulse ^{29}Si MAS NMR spectra for OH-bearing orthoenstatite.

For the orthoenstatite models containing OH defects in a Si or Mg vacancy, the δ_i^{Si} of Si sites that are directly linked (via oxygen) to the vacant site, or close to a H, are found to be most affected, whereas the δ_i^{Si} of more remote Si sites are within about ± 2 ppm of those in the ordered structure. This is consistent with the general knowledge that NMR

chemical shifts are less affected by more distant neighbors (cf., Stebbins and Xue 2014), and with our previous results on forsterite (Xue et al. 2017b).

Only the calculated NMR parameters for those Si sites that contribute most significantly to the simulated ^1H - ^{29}Si CP MAS NMR spectra of the energetically most favorable $(2\text{H})_{\text{M}2}$ model 1 and $(4\text{H})_{\text{SiB}}$ model 1 are individually listed in Table 4. The complete list for all the Si sites in these models, and those of the other orthoenstatite models can be found in supplementary Tables 3s and 4s.

$(2\text{H})_{\text{M}1}$ and $(2\text{H})_{\text{M}2}$ models

For the $(2\text{H})_{\text{M}2}$ defects, there are seven Si (3SiA, 4SiB) sites that are linked to a vacant M2 site (via oxygen), with one SiA site (Si32 in Table 4) linked by edge-sharing and the other Si sites by corner sharing (see supplementary Fig. 4s). In the $(2\text{H})_{\text{M}2}$ model 1, four of the Si sites (2SiA, 2SiB) adjacent to the vacant M2 site are bonded to one of the O2b, O2a, O1b

Table 4 ^{29}Si isotropic chemical shift (δ_i^{Si}), Si-H distance ($R(\text{Si-H})$), and estimated ^1H - ^{29}Si CP intensity (I_{CP}) for the defect-free and energetically most favorable defect models of MgSiO_3 orthoenstatite from FP calculation at 1 bar using the PBEsol and PBE functionals

Site number	Site type	Functional	δ_i^{Si} (ppm)	$\Delta\delta_i^{\text{Si}}$ (ppm) ^a	$R(\text{Si-H})(\text{\AA})$ ^b	I_{CP} ^c	Comment ^d
Defect-free orthoenstatite:							
17	SiA	PBEsol	-83.84	0			
		PBE	-83.31	0			
25	SiB	PBEsol	-80.07	0			
		PBE	-80.59	0			
$(2\text{H})_{\text{M}2}$ model 1							
32	SiA	PBEsol	-86.05	-2.22	2.252	79.0	SiA-(O3a- $V_{\text{M}2}$, O2a-H)
		PBE	-86.23	-2.92	2.242	80.7	SiA-(O3a- $V_{\text{M}2}$, O2a-H)
34	SiA	PBEsol	-81.59	2.25	2.462	47.0	SiA-O1a(- $V_{\text{M}2}$, \cdots H)
		PBE	-81.42	1.89	2.550	38.4	SiA-O1a(- $V_{\text{M}2}$, \cdots H)
48	SiB	PBEsol	-80.44	-0.37	2.301	69.0	SiB-O2b(- $V_{\text{M}2}$, H)
		PBE	-81.83	-1.24	2.288	70.9	SiB-O2b(- $V_{\text{M}2}$, H)
57	SiB	PBEsol	-78.75	1.32	2.607	34.0	SiB-O1b(- $V_{\text{M}2}$, \cdots H)
		PBE	-79.45	1.14	2.639	31.9	SiB-O1b(- $V_{\text{M}2}$, \cdots H)
$(4\text{H})_{\text{SiB}}$ model 1							
50	SiB	PBEsol	-73.44	6.63	2.299	84.0	SiB(Q1)-O3b(- V_{SiB} , H)
		PBE	-73.16	7.43	2.303	81.7	SiB(Q1)-O3b(- V_{SiB} , H)
54	SiB	PBEsol	-78.47	1.6	2.692	29.0	SiB on adjacent chain
		PBE	-78.60	1.99	2.746	26.1	SiB on adjacent chain
58	SiB	PBEsol	-74.46	5.61	2.19	106.0	SiB(Q1)-O3b(- V_{SiB} , H)
		PBE	-73.42	7.17	2.195	102.8	SiB(Q1)-O3b(- V_{SiB} , H)
61	SiB	PBEsol	-77.46	2.61	2.375	67.0	SiB on adjacent chain
		PBE	-77.53	3.06	2.431	58.9	SiB on adjacent chain

Note δ_i^{Si} is calculated from the isotropic chemical shielding (σ_i^{Si}) as the following: δ_i^{Si} (ppm) = σ_i^{Si} , ref + δ_i^{Si} , ref - σ_i^{Si} (ppm), where σ_i^{Si} , ref (429.675 ppm for the PBEsol, 433.00 ppm for the PBE functional) and δ_i^{Si} , ref (-81.95 ppm) are the average values for SiA and SiB in defect-free orthoenstatite

Only Si sites that are adjacent to the Si or Mg vacancy and have $R(\text{Si-H}) < 3 \text{ \AA}$ are enlisted

^a Difference in δ_i^{Si} from that calculated for the same Si site in defect-free orthoenstatite

^b Only $R(\text{Si-H}) < 3 \text{ \AA}$ shown

^c ^1H - ^{29}Si CP intensity calculated as the sum of $10^4 \times R(\text{Si-H})^{-6}$ for all H within 5 \AA of a given Si site. Note the scaling factor is arbitrary

^d $V_{\text{M}2}$: M2 vacancy; V_{SiB} : SiB vacancy

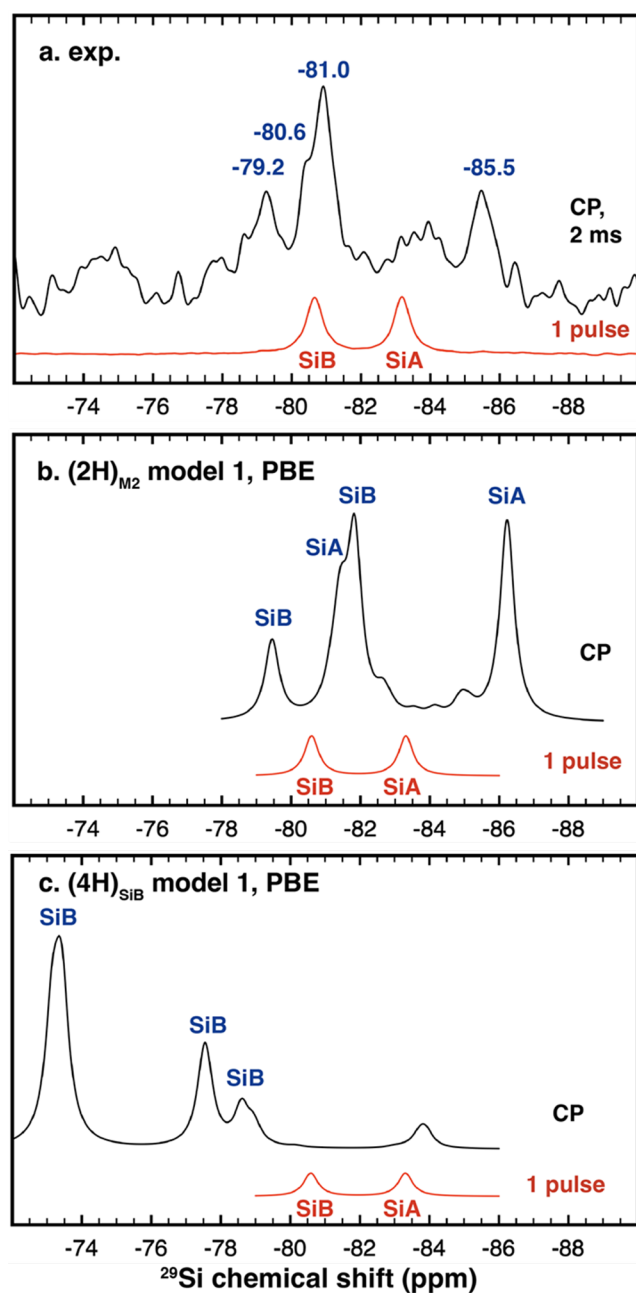


Fig. 8 ^1H - ^{29}Si CP MAS NMR spectrum at a contact time of 2 ms (same as Fig. 6e) (black curve), compared with single-pulse ^{29}Si MAS NMR spectrum (same as Fig. 6a) (red curve) for a hydrous MgSiO_3 orthoenstatite sample synthesized at 7 GPa and 1200 °C (a), and simulated ^1H - ^{29}Si CP MAS NMR spectra for the $(2\text{H})_{\text{M}2}$ model 1 (black curve) (b) and $(4\text{H})_{\text{SiB}}$ model 1 (black curve) (c) of MgSiO_3 orthoenstatite, compared with simulated single-pulse MAS NMR spectrum based on result for the defect-free orthoenstatite (red curve), from FP calculation at 1 bar using the PBE functional. For (b) and (c), a Lorentzian line broadening function of 0.5 ppm has been applied, and the relative intensities in the simulated CP spectra were taken to be proportional to the sum of $R(\text{Si-H})^{-6}$ to a given Si

and O1a in the $\text{O}2\text{a-H}\cdots\text{O}1\text{a}$ or $\text{O}2\text{b-H}\cdots\text{O}1\text{b}$ linkage, and show the shortest Si-H distances, and thus strongest ^1H - ^{29}Si CP intensities.

The simulated ^1H - ^{29}Si CP MAS NMR spectra for the $(2\text{H})_{\text{M}2}$ model 1 using the PBE and PBEsol functionals are shown in Fig. 8b and supplementary Fig. 18s. The δ_i^{Si} of the two SiA sites are shifted by +1.9/+2.3 ppm (PBE/PBEsol) and -2.9/-2.2 ppm (edge-sharing site), respectively, and that of the two SiB sites are shifted by +1.1/+1.3 and -1.2/-0.4 ppm, respectively, from the corresponding δ_i^{Si} value of the same site in the defect-free orthoenstatite. Compared with the observed ^1H - ^{29}Si CP MAS NMR spectrum at a short contact time of 2 ms for the hydrous orthoenstatite sample from this study (Fig. 8 and supplementary Fig. 18s), the overall features of four strongest peaks, with two on either side of the two peaks of SiA and SiB in the single-pulse MAS NMR spectrum (Si sites largely unaffected by OH defects), are well reproduced. Thus, the four strongest peaks experimentally observed near -79.2, -80.6, -81.0 and -85.5 ppm may be attributed to the four Si sites close to the $\text{O}2\text{a-H}\cdots\text{O}1\text{a}$ or $\text{O}2\text{b-H}\cdots\text{O}1\text{b}$ linkages (see Fig. 8a; Table 1).

On the other hand, the simulated CP MAS NMR spectrum of the less favorable $(2\text{H})_{\text{M}1}$ model 1, does not reproduce the peak of SiA shifted to more negative δ_i^{Si} (see supplementary Fig. 19s). Thus, the observed ^1H - ^{29}Si CP MAS NMR spectra for the hydrous orthoenstatite sample from this study match with that of the $(2\text{H})_{\text{M}2}$ model 1, but not the $(2\text{H})_{\text{M}1}$ model 1.

It should be noted that for the interpretation of ^{29}Si NMR spectra, often empirical correlations between the δ_i^{Si} and local structural parameters are applied. Such empirical interpretations would be difficult in the case of Mg vacancies, because there are no clear trends between the subtle changes of δ_i^{Si} and local structural parameters. Similar observations were made in our earlier study on forsterite (Xue et al. 2017b). FP calculations on model structures are thus particularly helpful.

$(4\text{H})_{\text{SiA}}$ and $(4\text{H})_{\text{SiB}}$ models

The simulated ^1H - ^{29}Si CP MAS NMR spectra for the $(4\text{H})_{\text{SiB}}$ model 1 using the PBE and PBEsol functionals are overall similar (see Fig. 8 and supplementary Fig. 20s). They are characterized by four (two of which overlapping with the PBE functional) relatively strong peaks that are shifted to the less negative δ_i^{Si} direction from the peak of SiB site in the single-pulse MAS NMR spectrum: two (overlapped into one with the PBE functional) stronger peaks shifted by 6–7 ppm, which originate from the two SiB sites that are adjacent to the vacant SiB site, and thus may be denoted as Q^1 (i.e., SiO_4 tetrahedron linked to one other tetrahedron), and

two weaker peaks that are shifted by a smaller amount (2–3 ppm), which are due to two SiB sites that are on adjacent silicate chains and remain Q² (i.e., SiO₄ tetrahedron linked to two other tetrahedra), but have relatively short Si-H distances (<3 Å). There are little contributions from the SiA sites.

The higher-energy (4H)_{SiB} models 2 and 4 also give simulated ¹H-²⁹Si CP MAS NMR spectra that show overall shift of the SiB peaks to less negative δ_i^{Si} direction (see supplementary Fig. 19s). The general trend of less negative δ_i^{Si} from Q² to Q¹ is qualitatively in accordance with empirical knowledge (cf., Stebbins and Xue 2014), although the more subtle changes for the SiB sites in adjacent silicate chains would be difficult to interpret empirically.

For the (4H)_{SiA} models, it is four SiA sites that are shifted to less negative δ_i^{Si} direction due to the presence of a SiA vacancy. Thus, the (4H)_{SiA} models overall predict ¹H-²⁹Si CP MAS NMR spectra that show peaks to more negative δ_i^{Si} direction, compared to those of the (4H)_{SiB} models (see supplementary Fig. 19s), rendering distinction of the two incorporation mechanisms with ¹H-²⁹Si CP MAS NMR possible.

If a hydrous orthoenstatite sample contains protons associated with Si vacancies, its ¹H-²⁹Si CP MAS NMR spectra at a short contact time are expected to resemble those shown in Fig. 8c and supplementary Fig. 20s for the (4H)_{SiB} model 1. The observed ¹H-²⁹Si CP MAS NMR spectra for the hydrous orthoenstatite sample from this study (see Figs. 6 and 8a) do not agree with the predicted spectrum, consistent with the lack of protons associated with Si vacancies in the sample.

Polarized infrared absorption spectra

(2H)_{M2} model 1

The calculated OH stretching frequencies (ν_{OH}) and IR intensities for the (2H)_{M2} model 1 are shown in Table 5. The simulated polarized IR spectra in the OH stretching region are compared with the experimental polarized IR absorption spectra of a hydrous MgSiO₃ orthoenstatite sample (En013c1) synthesized at 6 GPa and 1250 °C, described in Prechtel and Stalder (2010), which contain the two groups of bands (A1–A2 and A3–A4 bands), in Fig. 9. The (2H)_{M2} model 1 yielded two OH stretching bands with relatively low frequencies, at 3360 and 3161 cm⁻¹ using the PBE functional, and 3283 and 2929 cm⁻¹ using the PBEsol functional. The two sets of values are close to (bracketing) the A3 and A4 bands near 3362 and 3067 cm⁻¹ in the experimental IR spectra.

The stretching vibrations of the two O-H bonds in each mode are nearly decoupled: the band with a lower and higher wavenumber corresponds to the stretching vibration of the O2a-H and O2b-H bond with stronger and weaker hydrogen bonding, respectively (see Fig. 10a).

As is expected from the geometry (O-H nearly in the (001) plane), the intensities in the spectrum with the polarization along the *a* axis are nearly null, and the highest intensities are for the polarization along the *c* axis for both normal modes, which agree with that observed for the A3 and A4 bands (see Fig. 9a). The calculation results overall are consistent with that of Balan et al. (2013).

The orthoenstatite sample from the present study also exhibits two OH stretching bands corresponding to the A3

Table 5 OH stretching frequency and IR intensities (I_{IR}) of normal modes for the energetically most favorable defect models of MgSiO₃ orthoenstatite from FP calculation at 1 bar using the PBEsol and PBE functionals

Mode#	Functional	Frequency (cm ⁻¹)	I _{IR,x} (D ² Å ⁻² amu ⁻¹)	I _{IR,y} (D ² Å ⁻² amu ⁻¹)	I _{IR,z} (D ² Å ⁻² amu ⁻¹)	I _{IR,total} (D ² Å ⁻² amu ⁻¹)	I _{IR,total} (Lcm ⁻² /mol H ₂ O) ^a	Dominant displacements
(2H) _{M2} model 1								
482	PBEsol	2929.00	0.12	16.05	33.75	49.92	421,884	O2a-H1
	PBE	3160.97	0.11	12.18	24.36	36.64	309,691	O2a-H1
483	PBEsol	3283.00	0.01	7.32	23.39	30.72	259,621	O2b-H2
	PBE	3360.56	0.00	6.82	19.76	26.58	224,608	O2b-H2
(4H) _{SiB} model 1								
486	PBEsol	2237.00	0.20	79.78	4.48	84.46	713,788	O3b'-H4
	PBE	2617.42	0.47	64.63	4.39	69.49	587,298	O3b'-H4
487	PBEsol	2785.00	24.53	33.35	0.28	58.16	491,522	O3b-H1
	PBE	2972.08	20.55	28.62	0.11	49.29	416,563	O3b-H1
488	PBEsol	3520.00	6.14	0.21	1.71	8.06	68,117	O2b-H2
	PBE	3623.35	3.69	0.09	0.88	4.66	39,421	O2b-H2
489	PBEsol	3685.00	8.09	0.01	0.02	8.12	68,624	O1b-H3
	PBE	3735.12	6.68	0.03	0.00	6.71	56,712	O1b-H3

^a Calculated as I_{IR} (Lcm⁻²/mol H₂O) = 2 × I_{IR} (Lcm⁻²/mol OH) = 2 × 4225.6 × I_{IR} (D² Å⁻² amu⁻¹) (cf., Kendrick and Burnett 2016)

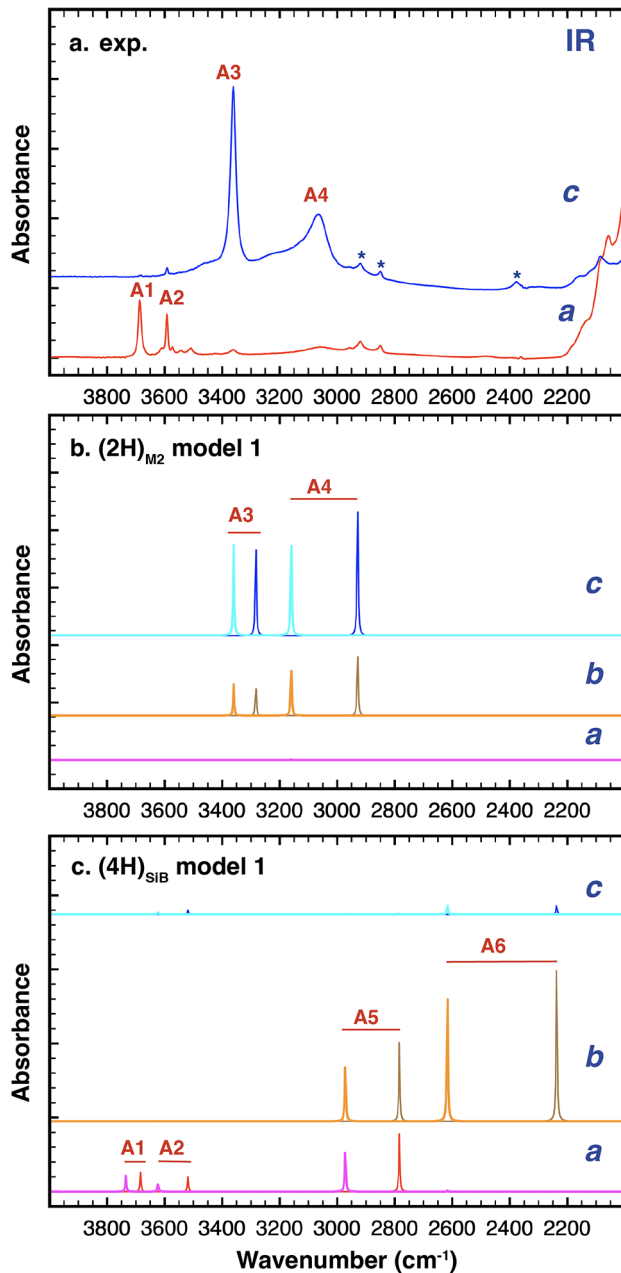
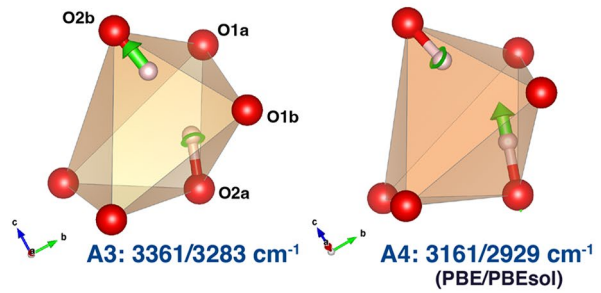


Fig. 9 Comparison of the polarized IR absorption spectra (without baseline correction) for the polarization parallel to the *c* and *a* axis (as labelled) on a MgSiO₃ orthoenstatite crystal (En013c1) synthesized at 6 GPa and 1250 °C, described in Prechtel and Stalder (2010)(a), with the simulated spectra for the polarization parallel to the *c*, *b* and *a* axis (as labelled) for the (2H)_{M2} model 1 (b) and (4H)_{SiB} model 1 (c) of MgSiO₃ orthoenstatite from FP calculation at 1 bar using the PBE (thick cyan, magenta and orange lines) and PBEsol (thin blue, brown and red lines) functionals. An arbitrary Lorentzian line broadening function of 4 cm⁻¹ has been applied to the simulated spectra. For (a), the spectra are plotted in a wider frequency range than that in the original publication (above 2950 cm⁻¹). The two small sharp bands near 2849 and 2920 cm⁻¹ (marked by asterisks) are due to epoxy resin. The small features in the region of 2300–2500 cm⁻¹ (marked by an asterisk) are likely due to imperfect subtraction of the signal from atmospheric CO₂. The bands below 2200 cm⁻¹ are consistent with those reported for overtones of lattice vibrations for orthoenstatite (cf., Prechtel and Stalder 2012)

a. (2H)_{M2} model 1



b. (4H)_{SiB} model 1

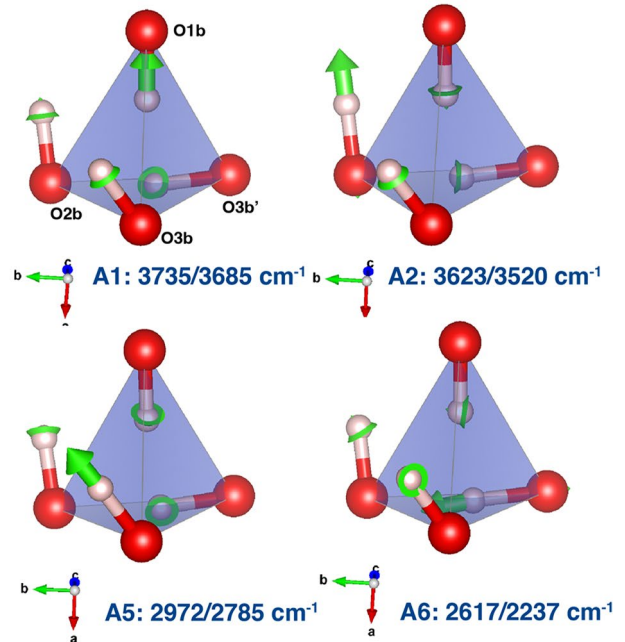


Fig. 10 OH stretching normal modes with the atomic displacements indicated by green arrows for the (2H)_{M2} model 1 (a) and (4H)_{SiB} model 1 (b) of MgSiO₃ orthoenstatite from FP calculation at 1 bar using the PBEsol functional, which are similar to those calculated using the PBE functional. The wavenumbers for each mode calculated using the PBE/PBEsol functionals are shown underneath (separated by a slash). A scaling factor of 0.6 has been applied to the calculated magnitude of displacements for clarity. The vacant octahedron and tetrahedron are also drawn as a guide to the eye. Drawn using the Vesta program (Momma and Izumi 2011)

and A4 bands. The attribution of the incorporated water to (2H)_{M2} defects for our sample has been unambiguously confirmed by NMR, lending further confidence to the assignment of these IR bands.

(4H)_{SiA} and (4H)_{SiB} models

The calculated OH stretching frequencies and IR intensities for the lowest-energy (4H)_{SiB} model 1 are tabulated in Table 5. The simulated polarized IR spectra are shown in Fig. 9c. As expected from the hydrogen bonding distances,

the calculated frequencies range from low to high, at 2617, 2972, 3623 and 3735 cm^{-1} using the PBE functional, and 2237, 2785, 3520 and 3684 cm^{-1} using the PBEsol functional. The two high-frequency bands are both strongly polarized along the *a* axis, the second lowest-frequency band is strongly polarized along the *a* and *b* axes, and the lowest-frequency band is strongly polarized along the *b* axis.

The stretching vibrations of the four O-H bonds are nearly decoupled, with the band from low to high frequency corresponding dominantly to the stretching vibration of O3b'-H, O3b-H, O2b-H and O1b-H, respectively (see Fig. 10b).

The IR spectra reported for hydrous orthoenstatite synthesized at low silica activities, including that shown in Fig. 9a, show two bands near 3687 and 3592 cm^{-1} (the A1 and A2 band), which are strongly polarized along the *a* axis (e.g., Grant et al. 2006; Prechtel and Stalder 2010). The two higher-frequency bands in the simulated spectrum of the (4H)_{SiB} model 1 (Fig. 9c) are in reasonable agreement, in both frequency and pleochroism, with these bands (Fig. 9a), with the experimental frequencies lying in between the two sets of values calculated using the two functionals (also see supplementary Fig. 21s). The calculated frequencies for the other two modes of the (4H)_{SiB} model 1 (denoted A5 and A6 in Fig. 9c) are both lower than those for the (2H)_{M2} model 1, and below the spectral range (generally above about 3000 cm^{-1}) of IR spectra reported for orthoenstatite (e.g., Prechtel and Stalder 2010; Stalder et al. 2012), due to stronger hydrogen bonding. Therefore, the predicted IR spectra for the (4H)_{SiB} model 1 can explain the A1 and A2 bands well, and further suggests that there are two lower-frequency bands that have been overlooked in IR studies thus far.

In order to examine whether the two lower-frequency bands for the (4H)_{SiB} defects could be detected experimentally, we plotted in Fig. 9a the experimental spectra for the orthoenstatite sample (En013c1) described in Prechtel and Stalder (2010) in a wider frequency range (4000–2000 cm^{-1}) than in the original publication. There are no clearly discernable band(s), other than those due to other sources (epoxy resin/atmospheric CO₂) and overtones of lattice vibrations below 3000 cm^{-1} , although the two spectra with different polarization directions have somewhat different shapes in the 3000–2200 cm^{-1} region.

It is well known that low-frequency OH stretching bands due to strongly hydrogen bonded OH groups tend to be very broad as a result of anharmonicity (e.g., Novak 1974). The trend of significant increase in band width with decreasing OH stretching frequency is also obvious from a visual inspection of the A1 and A2 bands vs. the A3 band vs. the A4 band in Fig. 9a. Therefore, the two lower-frequency A5 and A6 bands expected for the (4H)_{SiB} defects could be

even broader than the A4 band, to the extent to be difficult to detect at low concentrations. This was also noted by Balan et al. (2013) for the single low-frequency band predicted at 2615 and 2039 cm^{-1} for their two models similar to our (4H)_{SiB} model 4 and (4H)_{SiA} model 3.

It should be reminded that the simulated IR spectra from FP calculation shown here (Fig. 9b,c) have been plotted with an arbitrary band width, because the calculations do not carry any information regarding band width.

Below we attempt to make a more detailed comparison with nominally hydrous minerals of comparable hydrogen bonding (and δ_1^{H} , ν_{OH}) to gain better insights. It may be inferred that the lowest-frequency A6 band may be comparable in hydrogen bonding to dense hydrous magnesium silicate phase D, δ -AlOOH, and phase egg (with experimental δ_1^{H} of 12.0–12.5 ppm: Xue et al. (2006)). The OH stretching bands observed by Raman spectroscopy for all three minerals are very broad, ranging from 3000 to 1800–2000 cm^{-1} , with three maxima that may be caused by Fermi resonance with other vibrational modes. The lower-frequency part of the spectra were often not observed in earlier studies, partly due to difficulty of detecting weak, broad low-frequency bands (cf., Xue et al. 2006). It would thus be very difficult to detect at low concentrations.

The second lowest-frequency A5 band may be comparable in hydrogen bonding to α -AlOOH diaspore (with experimental δ_1^{H} of 9.4 ppm: Xue and Kanzaki (2007)). The reported IR spectra for the latter show OH stretching bands with maxima near 2995 and 2910 cm^{-1} , which are several hundred wavenumbers wide (e.g., Demichelis et al. 2007; Kohler et al. 1997; Stegmann et al. 1973), as compared to a FWHM of about 12 cm^{-1} for the A1 band in Fig. 9a. From our FP calculation (see Table 5; Fig. 9c), the A5 band is expected to yield little absorbance when the polarization is parallel to the *c* axis, and give an integrated absorbance that is about three times of that of the A1 band when the polarization is parallel to the *a* axis. The lack of a clearly discernable band in Fig. 9a below 3000 cm^{-1} are consistent with a much broader width (likely more than one order) for the A5 band than the A1 band. It is difficult to discern whether the different shapes in the region of 3000–2200 cm^{-1} between the two spectra with different polarization directions in Fig. 9a could be related to the existence of any extra broad band(s) in the spectrum along the *a* axis, or simply due to difference in baseline.

It should be noted that our IR spectrum for low-pressure clinoenstatite synthesized at 14 GPa and 1200 °C, for which both strong and weak hydrogen bonding were revealed by ¹H NMR, is dominated by high-frequency OH stretching bands, with no clearly recognizable bands

below 3000 cm^{-1} (Xue et al. 2018), supporting the above inference.

Thus, it may be concluded that the experimentally observed A1 and A2 bands for orthoenstatite may be attributed to the two high-frequency bands of $(4\text{H})_{\text{SiB}}$ defects. Two lower-frequency bands are also expected, but may be difficult to detect due to broadening associated with anharmonicity for strong hydrogen bonding.

There is a general correlation between the OH stretching frequency and hydrogen-bonding (O-H, $\text{H}\cdots\text{O}$ and $\text{O}\cdots\text{O}$) distances (see supplementary Fig. 26s), as has been known experimentally. A general correlation between the calculated total IR intensity (activity) and OH stretching frequency is also observed (see supplementary Fig. 27s), supporting the frequency dependency of IR absorption coefficient.

The energetically less favorable $(4\text{H})_{\text{SiB}}$ models 2 and 4 calculated using the PBEsol functional both yield three OH stretching bands at frequencies $> 3000\text{ cm}^{-1}$ (see supplementary Fig. 22s and 23s), inconsistent with the A1 and A2 bands, and another band with a low frequency (1942 or 2336 cm^{-1}). The simulated spectra for the $(4\text{H})_{\text{SiB}}$ model 4 resemble those for the $(4\text{H})_{\text{SiB}}$ model reported by Balan et al. (2013).

The calculated IR spectra for the energetically unfavorable $(4\text{H})_{\text{SiA}}$ models are described in detail in the supplementary material. For the $(4\text{H})_{\text{SiA}}$ model 1, a H-O-H bending vibration band near 1611 cm^{-1} is predicted because two of the H atoms are bonded to the same oxygen (O2a) (see supplementary Table 5s and Fig. 24s). As a band due to H-O-H bending vibration is commonly used as a characteristic feature for molecular H_2O , this finding is significant in that it presents yet another type of OH defects that also gives H-O-H bending vibration. It thus calls for caution of using this feature alone for the distinction of molecular H_2O and OH. For the $(4\text{H})_{\text{SiA}}$ model 2, the overall frequency distribution resembles, though not identical to, that of the $(4\text{H})_{\text{SiB}}$ model 1 (see supplementary Table 5s and Fig. 25s).

Discussion

Configurations and NMR and vibrational characteristics of $(2\text{H})_{\text{Mg}}$ and $(4\text{H})_{\text{Si}}$ defects in MgSiO_3 orthoenstatite

The combined ^1H and ^{29}Si NMR and vibrational spectroscopic measurements, and FP calculations allowed us to clarify the configurations and spectroscopic characteristics of $(2\text{H})_{\text{Mg}}$ and $(4\text{H})_{\text{Si}}$ defects in MgSiO_3 orthoenstatite.

For the $(2\text{H})_{\text{Mg}}$ defects in orthoenstatite, our study revealed that the most favorable configuration is the $(2\text{H})_{\text{M2}}$ model 1 with two inequivalent protons, one bonded to O2a pointing toward O1a, and another bonded to O2b pointing toward O1b. This defect produces two OH stretching bands near 3362 and 3067 cm^{-1} (A3 and A4 band, calculated: $3361/3283$ and $3161/2929\text{ cm}^{-1}$ with the PBE/PBEsol functional) that both yield higher intensities for the polarization direction along c and b axes than a axis. It yields two ^1H MAS NMR peaks near 5.9 and 7.6 ppm (calculated: $6.2/5.9$ and $7.2/8.0$ ppm with the PBE/PBEsol functional), which produce a pair of cross peaks in 2D ^1H NOESY and DQ MAS NMR spectra. Because of ^1H - ^1H dipolar coupling between the two protons, the ^1H MAS NMR spectra show a doublet with increasingly asymmetric and broader peak shape at lower spinning rates. The ^1H static NMR spectrum exhibits a moderate chemical shift range around 80 ppm.

For the $(4\text{H})_{\text{Si}}$ defects in orthopyroxene, our FP calculations predict that the $(4\text{H})_{\text{SiB}}$ model 1 is the most favorable configuration. The previously reported A1 and A2 bands near 3687 and 3592 cm^{-1} can be attributed to the two high-frequency bands for the $(4\text{H})_{\text{SiB}}$ model 1 (with corresponding calculated frequencies at $3735/3685$ and $3623/3520\text{ cm}^{-1}$ using the PBE/PBEsol functional), which are strongly polarized along a axis. This defect also gives two lower-frequency bands near $2972/2785\text{ cm}^{-1}$ (strongly polarized along b and a axes) and $2617/2237\text{ cm}^{-1}$ (strongly polarized along b axis), which are likely difficult to detect at low concentrations due to broadening associated with anharmonicity for strong hydrogen bonding.

In comparison, ^1H MAS NMR should be more straightforward in revealing all the OH species regardless of hydrogen bonding distance. The $(4\text{H})_{\text{SiB}}$ model 1 predicts four ^1H MAS NMR peaks near $1.0/1.2$, $1.6/1.1$, $8.9/9.3$ and $11.6/12.7$ ppm (using the PBE/PBEsol functional) with varying peak width (narrower for the two peaks with larger δ_{H}). The ^1H MAS NMR spectra for the $(4\text{H})_{\text{Si}}$ defects are expected to be overall broader than those of the $(2\text{H})_{\text{M2}}$ defects due to stronger dipolar ^1H - ^1H dipolar coupling within the 4H cluster. The ^1H static NMR spectrum is expected to span a large chemical shift range around 200 ppm with some narrow components in the middle due to O-H pointing away from the vacant tetrahedron.

One should also note that although OH defects in Mg and Si vacancies have been known to occur in a variety of minerals, the spectroscopic characteristics for a given type of OH defects, especially for those associated with Si vacancies, can vary largely depending on the crystal structure.

The $(4\text{H})_{\text{Si}}$ -type defects are often referred to as hydrogarnet substitution, as it was first noticed in hydrous grossular garnets $(\text{Ca}_3\text{Al}_2(\text{SiO}_4)_{3-x}(\text{O}_4\text{H}_4)_x)$ (Cohen-Addad et al. 1967). The hydrogarnet substitution has since been reported

to occur in a number of other silicate minerals, including garnets of other compositions, olivine, zircon, pyroxenes, coesite, and higher-pressure phases (cf., Smyth 2006).

For hydrogrossular, the four O-H bonds are known to be distributed close to the vacant tetrahedral faces (Lager et al. 1987, 1989). For Mg_2SiO_4 forsterite, FP calculations have shown that the most favorable configurations include one H on each oxygen of the vacant tetrahedron, with one H pointing away from the vacant tetrahedron and three others distributed along the vacant tetrahedral edges (Balan et al. 2011; Umemoto et al. 2011; Xue et al. 2017b). This study has shown that for orthoenstatite, there is also one H bonded to each of the four oxygen atoms on the vacant tetrahedron, but with two of the H pointing away from the vacant tetrahedron. The different 4H configurations render the ^1H - ^1H distances different, and thus ^1H static and MAS NMR spectra affected differently by homonuclear dipolar coupling. For hydrogarnet, a broad peak spanning about 200 ppm is observed in the ^1H static NMR spectra of katoite ($\text{Ca}_3\text{Al}_2(\text{O}_4\text{H}_4)_3$) and Si-bearing hydrogrossular (Xue et al. 2017a). In comparison, for hydrous forsterite, a broad component spanning a similar frequency range and a narrower component in the middle were observed, with the latter corresponding to the proton pointing away from the vacant tetrahedron (Xue et al. 2017b). This study revealed that orthoenstatite is also expected to yield a ^1H static NMR spectrum that has a broad component spanning a similar frequency range, overprinted by a narrower component.

More prominent are the different distributions in the hydrogen bonding distance (and δ_i^{H} and ν_{OH}) for hydrogarnet defects among the different minerals. For both hydrogarnet and forsterite, in which the SiO_4 tetrahedra are isolated from each other, the hydrogen bonding tends to be weak, because the OH is not bonded to any high-field strength Si. Thus, the δ_i^{H} for hydrogarnet (Xue et al. 2018) and hydrous forsterite (Xue et al. 2017b) are relatively small (both around 1–2 ppm). Their ν_{OH} are relatively high (e.g., 3600–3680 cm^{-1} for hydrogrossular with high water contents (e.g., Rossman and Aines 1991); > 3450 cm^{-1} for forsterite (e.g., Mosenfelder et al. 2006). In comparison, this study has shown that the hydrogen bonding for the hydrogarnet defects in orthoenstatite ranges from very weak to very strong, due to the presence of both bridging oxygen and nonbridging oxygen atoms, which result in both OH groups bonded to a Si (associated with O3b), and those bonded to no Si (associated with O1b/O2b). Therefore, two groups of ^1H NMR peaks for hydrogarnet defects in orthoenstatite with large (9–12 ppm) and small (~ 1 ppm) δ_i^{H} are expected. Similarly, two groups of OH stretching bands with high (observed: 3687 and 3592 cm^{-1} ; calculated: 3735/3685 and 3623/3520 cm^{-1} using the PBE/PBEsol functional) and low frequencies (calculated: 2972/2785 and 2617/2237 cm^{-1}) are expected. The

latter are likely difficult to observe at low concentrations due to broadening associated with anharmonicity.

Because the strength of hydrogen bonding may have significant effects on various physical properties, such as diffusivity and electrical conductivity, the revelation of the hitherto unexpected hydrogarnet defects with strong hydrogen bonding for orthoenstatite requires careful reconsideration of their effects on the physical properties.

Hydrogarnet defects in other mantle minerals with high Si/Mg ratios, such as the most abundant lower-mantle mineral, bridgmanite, may also form strong hydrogen bonding. It is thus important to investigate whether there are any OH defects in these minerals that may have been overlooked by IR spectroscopy.

Revised infrared absorption coefficients for orthoenstatite

There are large uncertainties in the IR absorption coefficients for OH stretching bands of nominally anhydrous minerals. For orthoenstatite, the universal wavenumber-dependent calibrations by Paterson (1982) and Libowitzky and Rossman (1997), and the mineral-specific calibration (Bell et al. 1995) based on natural orthoenstatite have often been adopted, which led to discrepancies in estimated water contents up to about a factor of 2 for samples containing dominantly $(2\text{H})_{\text{Mg}}$ defects (e.g., Rauch and Keppler 2002).

The revelation that only half of the expected OH stretching bands for the $(4\text{H})_{\text{Si}}$ defects in MgSiO_3 orthoenstatite have been detected by IR implies that the estimated water contents using either of these IR absorption coefficients would underestimate the true water content, when the $(4\text{H})_{\text{Si}}$ defects are present. Also, IR absorption coefficients calibrated on such samples against water contents determined independently by another method (e.g., SIMS), such as the modified wavelength-dependency reported for orthoenstatite by Stalder et al. (2012), need to be revised to take into consideration the undetected bands.

We derived the following revised absorption coefficients (I') for the two groups of bands using data from Stalder et al. (2012), by applying a correction factor of 2 to account for the undetected bands for the $(4\text{H})_{\text{Si}}$ defects (see supplementary material for details):

$$I'_{12} = 3.9(2) \text{ wt ppm}^{-1} \cdot \text{cm}^{-2} \text{ for the A1 + A2 band}$$

$$I'_{34} = 17.1(12) \text{ wt ppm}^{-1} \cdot \text{cm}^{-2} \text{ for the A3 + A4 band}$$

The obtained I'_{12}/I'_{34} ratio (0.23(2)) is comparable to the ratio (0.18/0.20 using the PBE/PBEsol functional) in the total IR intensity between the A1 + A2 bands and the A3 + A4 bands from FP calculation for the $(4\text{H})_{\text{SiB}}$ model 1 and $(2\text{H})_{\text{M2}}$ model 1, suggesting the results may be reasonable. Also, the derived I'_{34} is comparable to the value

(14.84(59) wt ppm⁻¹·cm⁻²) reported for natural orthoenstatite by Bell et al. (1995).

Incorporation mechanisms of water in MgSiO₃ orthoenstatite as a function of silica activity and pressure

The clarification of spectroscopic characteristics of different OH defects in MgSiO₃ orthoenstatite allowed us to interpret the available spectroscopic data in terms of changes in incorporation mechanisms of water in MgSiO₃ orthoenstatite as a function of silica activity and pressure.

The NMR and IR spectra of MgSiO₃ orthoenstatite synthesized at 7 GPa and 1200 °C using a starting material of stoichiometric Mg/Si ratio from this study are consistent with only (2H)_{Mg} defects. The IR spectra reported by Rauch and Keppeler (2002) for MgSiO₃ orthoenstatite synthesized at 0.2–7.5 GPa and 1100 °C using a starting material of nearly stoichiometric Mg/Si ratio with slight excess silica similarly are consistent with (2H)_{Mg} defects. On the other hand, the IR spectra by Stalder and coauthors (e.g., Prechtel and Stalder 2010; Stalder et al. 2012) on MgSiO₃ orthoenstatite synthesized under different pressure (4–8 GPa) and silica activity conditions (with starting Mg/Si ratio ranging from 60/40 to 45/55) revealed four bands, among which the A1 and A2 bands can now be attributed to the two high-frequency bands of the (4H)_{Si} defects, and the A3 and A4 bands to the (2H)_{Mg} defects with confidence. Their reported changes in the relative integrated absorbances can be ascribed to increasing proportion of OH defects in Si vacancies than those in Mg vacancies with increasing pressure and decreasing silica activity.

Note that there are some inconsistencies in the reported relative integrated absorbances of the A1 to A4 bands for samples synthesized under similar conditions between studies from different groups, or even within the same group. This may be caused by different baseline correction methods for the IR spectra and/or experimental complications (e.g., sample preparation procedure, chemical heterogeneity, temperature fluctuation/difference). Careful quantification of the relative abundances of different OH defects under different conditions is needed for thermodynamic modelling of water incorporation in mantle minerals.

Conclusions

Our hydrous MgSiO₃ orthoenstatite sample synthesized at 7 GPa and 1200 °C using a starting material of stoichiometric Mg/Si ratio was confirmed to contain only (2H)_{M2} defects (a pair of protons in a Mg (M2) vacancy), which are characterized by two narrow ¹H MAS NMR peaks near 5.9 and 7.6 ppm that are correlated in 2D ¹H NMR spectra, and two

OH stretching bands near 3361 and 3066 cm⁻¹ that match with the A3 and A4 IR bands reported previously. All the ¹H MAS and static NMR, ¹H-²⁹Si CP MAS NMR spectra, and IR spectra were well reproduced by FP calculations for the (2H)_{M2} model.

Our FP calculations also revealed that the previously reported A1 and A2 bands near 3687 and 3592 cm⁻¹ for orthoenstatite synthesized at lower silica activities can be attributed to the two OH stretching bands associated with O1b/O2b (calculated: 3735/3685 and 3623/3520 cm⁻¹ using the PBE/PBEsol functional) for the (4H)_{SiB} defects (four protons in a SiB vacancy). Two other bands with lower frequencies (calculated: 2972/2785 and 2617/2237 cm⁻¹) that are associated with the two bridging oxygen atoms (O3b) are also expected. They are outside the frequency range of IR spectra for orthoenstatite reported thus far, and are likely difficult to observe because of broadening associated with anharmonicity for strong hydrogen bonding. The (4H)_{SiB} defects are expected to yield four ¹H MAS NMR peaks with both small and large chemical shifts (calculated: 1.6/1.1, 1.0/1.2, 8.9/9.3 and 11.6/12.7 ppm using the PBE/PBEsol functional) and varying peak widths, and ¹H static NMR spectrum spanning a wide frequency range of about 200 ppm with narrow features on top. ¹H NMR should be more effective in quantitatively identifying all the protons.

The finding of undetected IR bands for OH defects in orthoenstatite requires revision of the IR absorption coefficients reported thus far. We derived a set of revised absorption coefficients for the two groups of IR bands using data reported previously, by applying a correction factor to account for the undetected bands.

The clarification of spectroscopic features allowed us to interpret the available data of orthoenstatite in terms of increasing proportion of OH defects in Si vacancies than those in Mg vacancies with increasing pressure and decreasing silica activity.

Finally, this study demonstrated the effectiveness of combined multi-nuclear NMR and vibrational spectroscopic measurements and FP calculations in clarifying the nature of OH defects in minerals. The finding that IR spectroscopy, the most widely used method, may fail to detect OH defects, and thus underestimate the true water contents, in case of strong hydrogen bonding, could have implications well beyond enstatite.

Supplementary Information The online version contains supplementary material available at <https://doi.org/10.1007/s00410-024-02114-3>.

Acknowledgements We thank Jianjun Jiang and Shigeru Yamashita for assistance with the FT-IR measurement and discussion, Yusuke Yachi and Tsutomu Ota for assistance with the EPMA analysis, and Roland Stalder for providing the data of polarized FT-IR spectra shown in Fig. 9a, which were remeasured for a hydrous orthoenstatite crystal

(En013c1) described in Prechtel and Stalder (2010), and for discussion on the data. We also thank two anonymous reviewers for constructive comments, and Hans Keppler and Dante Canil for editorial handling. Part of this study was carried out during the Misasa International Student Intern Program (MISIP) 2016 (participated by A.-E. D. and C. G.), which was supported by a “Special Expenditure” funded by the Ministry of Education, Culture, Sports, Science and Technology (MEXT), Japan. This study was partly supported by the Japan Society for the Promotion of Science (JSPS) grant Kiban-A, No. 17H01174 to X.X.

Author contributions X. X. and M. K. are the principle responsible persons for the conception and design of the study. X. X. is the principle responsible person for the NMR measurements and first-principles calculations, and M. K. is the principle responsible person for the sample synthesis and Raman measurement. A.-E. D. and C. G. participated in the initial phase of the study (sample synthesis and preliminary study of NMR/Raman/EPMA measurements and first-principles calculations) during the MISIP 2016 program. The first draft of the manuscript was written by X. X., and all authors commented on previous versions of the manuscript. All authors read and approved the final manuscript.

Funding Open Access funding provided by Okayama University.

Declarations

Conflict of interest The author declares that the submitted work does not bear any conflict of interest.

Open Access This article is licensed under a Creative Commons Attribution 4.0 International License, which permits use, sharing, adaptation, distribution and reproduction in any medium or format, as long as you give appropriate credit to the original author(s) and the source, provide a link to the Creative Commons licence, and indicate if changes were made. The images or other third party material in this article are included in the article’s Creative Commons licence, unless indicated otherwise in a credit line to the material. If material is not included in the article’s Creative Commons licence and your intended use is not permitted by statutory regulation or exceeds the permitted use, you will need to obtain permission directly from the copyright holder. To view a copy of this licence, visit <http://creativecommons.org/licenses/by/4.0/>.

References

- Ashbrook SE, Berry AJ, Frost DJ, Gregorovic A, Pickard CJ, Readman JE, Wimperis S (2007) ^{17}O and ^{29}Si NMR parameters of MgSiO_3 phases from high-resolution solid-state NMR spectroscopy and first-principles calculations. *J Am Chem Soc* 129(43):13213–13224. <https://doi.org/10.1021/ja074428a>
- Bak M, Rasmussen JT, Nielsen NC (2000) SIMPSON: a general simulation program for solid-state NMR. *Spectrosc J Magn Reson* 147:296–330
- Balan E, Ingrin J, Delattre S, Kovacs I, Blanchard M (2011) Theoretical infrared spectrum of OH-defects in forsterite. *Eur J Mineral* 23(3):285–292. <https://doi.org/10.1127/0935-1221/2011/0023-2090>
- Balan E, Blanchard M, Yi H, Ingrin J (2013) Theoretical study of OH-defects in pure enstatite. *Phys Chem Minerals* 40(1):41–50. <https://doi.org/10.1007/s00269-012-0544-6>
- Bell DR, Ihinger PD, Rossman GR (1995) Quantitative analysis of trace OH in garnet and pyroxenes. *Am Mineral* 80(5–6):465–474
- Bromiley GD, Bromiley FA (2006) High-pressure phase transitions and hydrogen incorporation into MgSiO_3 enstatite. *Am Mineral* 91(7):1094–1101. <https://doi.org/10.2138/am.2006.2020>
- Brown ID (2002) The chemical bond in inorganic chemistry: the bond valence model. Oxford Science
- Cohen-Addad C, Ducros P, Bertaut EF (1967) Etude de la substitution Du Groupement SiO_4 par $(\text{OH})_4$ dans les composés $\text{Al}_2\text{Ca}_3(\text{OH})_{12}$ et $\text{Al}_2\text{Ca}_3(\text{SiO}_4)_{2,16}(\text{OH})_{3,36}$ De type grenat. *Acta Crystallogr* 23(2):220–230. <https://doi.org/10.1107/S0365110X67002518>
- Dal Corso A (2014) Pseudopotentials periodic table: from H to Pu. *Comput Mater Sci* 95:337–350. <https://doi.org/10.1016/j.commatsci.2014.07.043>
- Demichelis R, Noel Y, Civalleri B, Roetti C, Ferrero M, Dovesi R (2007) The vibrational spectrum of α - AlOOH diaspro: an ab initio study with the CRYSTAL code. *J Phys Chem B* 111(31):9337–9346. <https://doi.org/10.1021/jp072501d>
- Giannozzi P, Baroni S, Bonini N, Calandra M, Car R, Cavazzoni C, Ceresoli D, Chiarotti GL, Cococcioni M, Dabo I, Corso AD, Gironcoli Sd, Fabris S, Fratesi G, Gebauer R, Gerstmann U, Gougousis C, Kokalj A, Lazzeri M, Martin-Samos L, Marzari N, Mauri F, Mazzarello R, Paolini S, Pasquarello A, Paulatto L, Sbraccia C, Scandolo S, Sclauzero G, Seitsonen AP, Smogunov A, Umari P, Wentzcovitch RM (2009) QUANTUM ESPRESSO: a modular and open-source software project for quantum simulations of materials. *J Phys: Condens Matter* 21(39):395502
- Giannozzi P, Andreussi O, Brumme T, Bunau O, Nardelli MB, Calandra M, Car R, Cavazzoni C, Ceresoli D, Cococcioni M, Colonna N, Carnimeo I, Dal Corso A, de Gironcoli S, Delugas P, DiStasio RA, Ferretti A, Floris A, Fratesi G, Fugallo G, Gebauer R, Gerstmann U, Giustino F, Gorni T, Jia J, Kawamura M, Ko HY, Kokalj A, Kucukbenli E, Lazzeri M, Marsili M, Marzari N, Mauri F, Nguyen NL, Nguyen HV, Otero-de-la-Roza A, Paulatto L, Ponce S, Rocca D, Sabatini R, Santra B, Schlipf M, Seitsonen AP, Smogunov A, Timrov I, Thonhauser T, Umari P, Vast N, Wu X, Baroni S (2017) Advanced capabilities for materials modelling with QUANTUM ESPRESSO. *J Phys: Condens Matter* 29(46). <https://doi.org/10.1088/1361-648X/aa8f79>
- Grant KJ, Kohn SC, Brooker RA (2006) Solubility and partitioning of water in synthetic forsterite and enstatite in the system $\text{MgO}-\text{SiO}_2-\text{H}_2\text{O} \pm \text{Al}_2\text{O}_3$. *Contrib Mineral Petrol* 151(6):651–664. <https://doi.org/10.1007/s00410-006-0082-7>
- Ingrin J, Blanchard M (2006) Diffusion of hydrogen in minerals. *Rev Mineral Geochem* 62:291–320. <https://doi.org/10.2138/rmg.2006.62.13>
- Jacobsen SD (2006) Effect of water on the equation of state of nominally anhydrous minerals. *Rev Mineral Geochem* 62:321–342. <https://doi.org/10.2138/rmg.2006.62.14>
- Juhl DW, Tosner Z, Vosegaard T (2020) Versatile NMR simulations using SIMPSON. In: Webb GA (ed) *Annu Rep NMR Spectrosc*, vol 100. pp 1–59
- Kanzaki M, Xue XY (2017) Protoenstatite in MgSiO_3 samples prepared by conventional solid state reaction. *J Mineral Petrol Sci* 112(6):359–364. <https://doi.org/10.2465/jmps.170616>
- Karato S (2006) Remote sensing of hydrogen in Earth’s mantle. *Rev Mineral Geochem* 62:343–376. <https://doi.org/10.2138/rmg.2006.62.15>
- Kendrick J, Burnett AD (2016) PDIELEC: the calculation of infrared and terahertz absorption for powdered crystals. *J Comput Chem* 37(16):1491–1504. <https://doi.org/10.1002/jcc.24344>
- Keppler H, Smyth JR (2006) Water in nominally anhydrous minerals. *Rev Mineral Geochem*, vol 62. Mineralogical Society of America, Chantilly, Virginia
- Kohler T, Armbruster T, Libowitzky E (1997) Hydrogen bonding and Jahn-Teller distortion in groutite, α - MnOOH , and manganite, γ - MnOOH , and their relations to the manganese dioxides ramsdellite and pyrolusite. *J Solid State Chem* 133(2):486–500

- Kohn SC (1996) Solubility of H₂O in nominally anhydrous mantle minerals using ¹H MAS NMR. *Am Mineral* 81(11–12):1523–1526
- Lager GA, Armbruster T, Faber J (1987) Neutron and X-ray diffraction study of hydrogarnet Ca₃Al₂(O₄H₄)₃. *Am Mineral* 72:756–765
- Lager GA, Armbruster T, Rotella FJ, Rossman GR (1989) OH substitution in garnets: X-ray and neutron diffraction, infrared, and geometric-modeling studies. *Am Mineral* 74:840–851
- Libowitzky E, Rossman GR (1997) An IR absorption calibration for water in minerals. *Am Mineral* 82:1111–1115
- Momma K, Izumi F (2011) VESTA 3 for three-dimensional visualization of crystal, volumetric and morphology data. *J Appl Crystallogr* 44:1272–1276
- Mosenfelder JL, Deligne NI, Asimow PD, Rossman GR (2006) Hydrogen incorporation in olivine from 2–12 GPa. *Am Mineral* 91(2–3):285–294. <https://doi.org/10.2138/am.2006.1943>
- Novak A (1974) Hydrogen bonding in solids. Correlation of spectroscopic and crystallographic data. In: Dunitz JD, Hemerich P, Holm RH, Ibers JA, Jorgensen CK, Neilands JB, Reimene D, Williams RJP (eds) *Structure and bonding: large molecules*. vol. 18. Springer, New York, pp 177–216
- Ohtani E (2021) Hydration and dehydration in Earth's interior. In: Jeanloz R, Freeman KH (eds) *Ann Rev Earth Planet Sci*, Vol 49, 2021, vol 49. pp 253–278
- Pacalo REG, Gasparik T (1990) Reversals of the orthoenstatite-clinoenstatite transition at high pressures and high temperatures. *J Geophys Res* 95:15853–15858
- Paterson MS (1982) The determination of hydroxyl by infrared-absorption in quartz, silicate-glasses and similar materials. *Bull Mineral* 105(1):20–29
- Perdew JP, Burke K, Ernzerhof M (1996) Generalized gradient approximation made simple. *Phys Rev Lett* 77(18):3865–3868
- Perdew JP, Ruzsinszky A, Csonka GI, Vydrov OA, Scuseria GE, Constantin LA, Zhou X, Burke K (2008) Restoring the density-gradient expansion for exchange in solids and surfaces. *Phys Rev Lett* 100(13):136406
- Peslier AH, Schonbachler M, Busemann H, Karato SI (2017) Water in the Earth's interior: distribution and origin. *Space Sci Rev* 212(1–2):743–810. <https://doi.org/10.1007/s11214-017-0387-z>
- Phillips BL, Burnley PC, Warminghaus K, Navrotsky A (1997) ²⁹Si and ¹H NMR spectroscopy of high-pressure hydrous magnesium silicates. *Phys Chem Minerals* 24:179–190
- Pickard CJ, Mauri F (2001) All-electron magnetic response with pseudopotentials: NMR chemical shifts. *Phys Rev B* 63(24):245101. <https://doi.org/10.1103/PhysRevB.63.245101>
- Prechtel F, Stalder R (2010) FTIR spectroscopy with a focal plane array detector: a novel tool to monitor the spatial OH-defect distribution in single crystals applied to synthetic enstatite. *Am Mineral* 95(5–6):888–891. <https://doi.org/10.2138/am.2010.3497>
- Prechtel F, Stalder R (2011) The potential use of OH-defects in enstatite as geobarometer. *Contrib Mineral Petrol* 162(3):615–623. <https://doi.org/10.1007/s00410-011-0615-6>
- Prechtel F, Stalder R (2012) OH-defects in Al- and Cr- doped synthetic enstatites and defect geobarometry on natural orthopyroxenes from the Earth's mantle. *Eur J Mineral* 24(3):471–481. <https://doi.org/10.1127/0935-1221/2012/0024-2208>
- Rauch M, Keppler H (2002) Water solubility in orthopyroxene. *Contrib Mineral Petrol* 143(5):525–536. <https://doi.org/10.1007/s00410-002-0365-6>
- Rossman GR, Aines RD (1991) The hydrous components in garnets - grossular-hydrogrossular. *Am Mineral* 76(7–8):1153–1164
- Sakurai M, Tsujino N, Sakuma K, Kawamura K, Takahashi E (2014) Determination of H positions in orthoenstatite from IR spectra. *J Comput Chem Jpn* 13:169–170 (In Japanese)
- Smyth JR (2006) Hydrogen in high pressure silicate and oxide mineral structures. *Rev Mineral Geochem* 62:85–115. <https://doi.org/10.2138/rmg.2006.62.5>
- Stalder R, Prechtel F, Ludwig T (2012) No site-specific infrared absorption coefficients for OH-defects in pure enstatite. *Eur J Mineral* 24(3):465–470. <https://doi.org/10.1127/0935-1221/2012/0024-2180>
- Stebbins JF, Xue X (2014) NMR spectroscopy of inorganic Earth materials. *Rev Mineral Geochem* 78(1):605–653. <https://doi.org/10.2138/rmg.2014.78.15>
- Stegmann MC, Vivien D, Mazieres C (1973) Etude des modes de vibration infrarouge dans les oxyhydroxydes d'aluminium boehmite et diaspore. *Spectrochimica Acta Part A: Mol Spectrosc* 29(8):1653–1663. [https://doi.org/10.1016/0584-8539\(73\)80115-1](https://doi.org/10.1016/0584-8539(73)80115-1)
- Umemoto K, Wentzcovitch RM, Hirschmann MM, Kohlstedt DL, Withers AC (2011) A first-principles investigation of hydrous defects and IR frequencies in forsterite: the case for Si vacancies. *Am Mineral* 96(10):1475–1479. <https://doi.org/10.2138/am.2011.3720>
- Withers AC, Hirschmann MM (2007) H₂O storage capacity of MgSiO₃ clinoenstatite at 8–13 GPa, 1,100–1,400°C. *Contrib Mineral Petrol* 154(6):663–674. <https://doi.org/10.1007/s00410-007-0215-7>
- Xue X, Kanzaki M (2004) Dissolution mechanisms of water in depolymerized silicate melts: constraints from ¹H and ²⁹Si NMR spectroscopy and ab initio calculations. *Geochim Cosmochim Acta* 68(24):5027–5057
- Xue X, Kanzaki M (2007) High-pressure δ-Al(OH)₃ and δ-AlOOH phases and isostructural hydroxides/oxyhydroxides: new structural insights from high-resolution ¹H and ²⁷Al NMR. *J Phys Chem B* 111:13156–13166
- Xue X, Kanzaki M (2009) Proton distributions and hydrogen bonding in crystalline and glassy hydrous silicates and related inorganic materials: insights from high-resolution solid-state NMR spectroscopy. *J Am Ceram Soc* 92(12):2803–2830
- Xue X, Kanzaki M (2024) Correlation between Si-Al disorder and hydrogen-bonding distance variation in ussingite (Na₂AlSi₃O₈OH) revealed by one- and two-dimensional multi-nuclear NMR and first-principles calculation. *Am Mineral* in press
- Xue X, Kanzaki M, Fukui H, Ito E, Hashimoto T (2006) Cation order and hydrogen bonding of high-pressure phases in the Al₂O₃-SiO₂-H₂O system: an NMR and Raman study. *Am Mineral* 91:850–861
- Xue X, Kanzaki M, Shatskiy A (2008) Dense hydrous magnesium silicates, phase D and superhydrous B: new structural constraints from one- and two- dimensional ²⁹Si and ¹H NMR. *Am Mineral* 93:1099–1111
- Xue X, Kanzaki M, Geiger AC (2017a) Hydrogen incorporation mechanism in synthetic katoite-grossular and natural grossular: ¹H static and MAS NMR and first-principles calculation. Goldschmidt conference 2017 abstract
- Xue X, Kanzaki M, Turner D, Loroch D (2017b) Hydrogen incorporation mechanisms in forsterite: new insights from ¹H and ²⁹Si NMR spectroscopy and first-principles calculation. *Am Mineral* 102(3):519–536
- Xue X, Kanzaki M, Jiang J (2018) Incorporation mechanisms of hydrogen in enstatite. Japan Geoscience Union (JpGU) 2018 annual meeting abstract
- Yoshino T, Katsura T (2013) Electrical conductivity of mantle minerals: Role of water in conductivity anomalies. In: Jeanloz R (ed) *Annual Review of Earth and Planetary Sciences*, vol 41. pp 605–628